



# Simultaneous determination of mass-dependent Mg isotopic variations and radiogenic $^{26}\text{Mg}$ by laser ablation-MC-ICP-MS and implications for the formation of chondrules

Zhengbin Deng, Marc Chaussidon, Denton S. Ebel, Johan Villeneuve, Julien Moureau, Frédéric Moynier

## ► To cite this version:

Zhengbin Deng, Marc Chaussidon, Denton S. Ebel, Johan Villeneuve, Julien Moureau, et al.. Simultaneous determination of mass-dependent Mg isotopic variations and radiogenic  $^{26}\text{Mg}$  by laser ablation-MC-ICP-MS and implications for the formation of chondrules. *Geochimica et Cosmochimica Acta*, 2021, 10.1016/j.gca.2021.01.015 . insu-03130968

**HAL Id: insu-03130968**

**<https://insu.hal.science/insu-03130968>**

Submitted on 4 Feb 2021

**HAL** is a multi-disciplinary open access archive for the deposit and dissemination of scientific research documents, whether they are published or not. The documents may come from teaching and research institutions in France or abroad, or from public or private research centers.

L'archive ouverte pluridisciplinaire **HAL**, est destinée au dépôt et à la diffusion de documents scientifiques de niveau recherche, publiés ou non, émanant des établissements d'enseignement et de recherche français ou étrangers, des laboratoires publics ou privés.

## Journal Pre-proofs

Simultaneous determination of mass-dependent Mg isotopic variations and radiogenic  $^{26}\text{Mg}$  by laser ablation-MC-ICP-MS and implications for the formation of chondrules

Zhengbin Deng, Marc Chaussidon, Denton S. Ebel, Johan Villeneuve, Julien Moureau, Frédéric Moynier

PII: S0016-7037(21)00037-5  
DOI: <https://doi.org/10.1016/j.gca.2021.01.015>  
Reference: GCA 12045

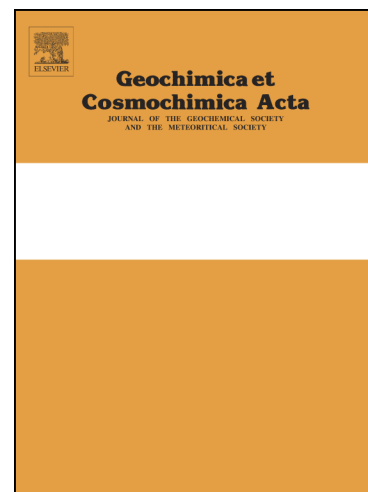
To appear in: *Geochimica et Cosmochimica Acta*

Received Date: 10 April 2019  
Revised Date: 13 January 2021  
Accepted Date: 15 January 2021

Please cite this article as: Deng, Z., Chaussidon, M., Ebel, D.S., Villeneuve, J., Moureau, J., Moynier, F., Simultaneous determination of mass-dependent Mg isotopic variations and radiogenic  $^{26}\text{Mg}$  by laser ablation-MC-ICP-MS and implications for the formation of chondrules, *Geochimica et Cosmochimica Acta* (2021), doi: <https://doi.org/10.1016/j.gca.2021.01.015>

This is a PDF file of an article that has undergone enhancements after acceptance, such as the addition of a cover page and metadata, and formatting for readability, but it is not yet the definitive version of record. This version will undergo additional copyediting, typesetting and review before it is published in its final form, but we are providing this version to give early visibility of the article. Please note that, during the production process, errors may be discovered which could affect the content, and all legal disclaimers that apply to the journal pertain.

© 2021 Published by Elsevier Ltd.



**Simultaneous determination of mass-dependent Mg isotopic variations and radiogenic  $^{26}\text{Mg}$  by laser ablation-MC-ICP-MS and implications for the formation of chondrules**

Zhengbin Deng<sup>a\*†</sup>, Marc Chaussidon<sup>a</sup>, Denton S. Ebel<sup>a,b,c</sup>, Johan Villeneuve<sup>d</sup>, Julien Moureau<sup>a</sup>, Frédéric Moynier<sup>a</sup>

<sup>a</sup>Université de Paris, Institut de physique du globe de Paris, CNRS, UMR 7154, Paris 75005, France.

<sup>b</sup>Department of Earth and Planetary Sciences, American Museum of Natural History, New York, New York, USA.

<sup>c</sup>Department of Earth and Environmental Sciences, Columbia University, New York, USA.

<sup>d</sup>Centre de Recherches Pétrographiques et Géochimiques, Université de Lorraine, CNRS 7358, Vandoeuvre-lès-Nancy, France.

\*Corresponding author: zhengbin.deng@sund.ku.dk

†Present address: Centre for Star and Planet Formation, Globe Institute, University of Copenhagen, Copenhagen, Denmark.

**Abstract**

Improvements in our understanding of the formation of chondrules requires a better knowledge of the thermal histories and the nature of their solid precursors. We present an *in situ* nanosecond laser ablation multi-collector inductively-coupled-plasma mass-spectrometry (LA-MC-ICP-MS) technique to measure simultaneously mass-dependent Mg isotopic fractionations and radiogenic  $^{26}\text{Mg}$  in chondritic components, thus allowing us to investigate

within a chronological framework the thermal processes redistributing Mg in chondrules and their precursors. The internal  $^{26}\text{Al}$ - $^{26}\text{Mg}$  isochrons provide initial  $^{26}\text{Al}/^{27}\text{Al}$  ratios from  $5.46 (\pm 0.38) \times 10^{-5}$  to  $6.14 (\pm 0.92) \times 10^{-5}$  for amoeboid olivine aggregates (AOAs) and Ca-, Al-rich inclusions (CAIs), and from  $0.16 (\pm 0.08) \times 10^{-5}$  to  $1.87 (\pm 0.92) \times 10^{-5}$  for chondrules from Allende and Leoville chondrites, which are consistent with the previously reported values. The combination of these values with up to 2.5‰ variation of the  $^{25}\text{Mg}/^{24}\text{Mg}$  ratio within the studied chondrules shows that: (i) AOAs and the precursors of chondrules were likely formed via condensation of rapid-cooling gas reservoirs, and (ii) Mg stable isotopes are probably at disequilibrium between olivines and mesostases in some chondrules, likely due to Mg loss by vaporization during chondrule formation. We use these new observations to propose that Mg isotopes can likely serve as a tracer for the thermal histories of chondrules. We present here a scenario taking into account Mg loss by vaporization from chondrule melt and Mg gain into the melt by olivine dissolution. The existing Mg isotopic observations in chondrule melts and olivines can be explained in a scenario with a homogeneous distribution of Mg isotopes and initial  $^{26}\text{Al}$  in the accretion disk, provided that chondrule precursors have been heated up to sufficiently high peak temperatures (up to 2123 K) and stayed above 1800 K for several tens of minutes to allow for significant Mg evaporation. These conditions are most consistent with a shock wave model for the origin of chondrules.

## 1. Introduction

Chondrules are near-spherical objects forming a large fraction of primitive chondrites.

Ordinary chondrules are hundreds of microns to several centimeters in size (Friedrich et al., 2015), and are composed of olivine, pyroxene and glassy silicates (also referred as mesostasis phases), indicating that they were once partially or totally molten before being quenched (e.g., Jones and Scott, 1989; Connolly and Love, 1998; Hewins and Fox, 2004; Krot et al., 2009; Ebel et al., 2018; Russell et al., 2018). The origin of chondrules is a long-standing question. Various sources of heating have been proposed to be responsible for chondrule formation, e.g., nebula lightning in the disk, solar flares, accretion shock waves, planetesimal bow shocks, and collisions between planetesimals (e.g., Asphaug et al. 2011; Desch et al., 2012; Connolly and Jones, 2016; Russell et al., 2018; Morris and Boley, 2018). Whether these heating processes can or cannot produce the thermal histories observed for chondrules, is a key criterion to discriminate between these different models (Desch et al., 2012; Connolly and Jones, 2016). This is one of the reasons why a multitude of experiments have been carried out on chondrule analogs to reproduce either textures or chemical features of chondrules (e.g., Hewins and Radomsky, 1990; Connolly and Love, 1998; Connolly and Jones, 2016; and references therein). However, the thermal histories proposed for chondrules in literature remain quite diverse with cooling rates spanning from several to thousands of degrees per hour and peak temperatures varying between  $< 1800$  K and  $\approx 2200$  K (Desch et al., 2012; and references therein). To trace the heat sources at the origin of chondrules, it would be necessary to reconstruct as well as possible the thermal histories of chondrules.

In addition to the thermal history, the nature of the precursors of chondrules is also yet largely unknown. Based on *in situ* secondary ion mass spectrometry (SIMS) oxygen isotopic

analyses, the presence in type I chondrules of relict Mg-rich olivines that are enriched in  $^{16}\text{O}$  relative to other coexisting olivines, pyroxene and mesostases in chondrules and therefore did not equilibrate with the melt have been discovered (Weinbruch et al., 1993; Jones et al., 2004; Pack et al., 2004; Chaussidon et al., 2008; Rudraswami et al., 2011; Libourel and Chaussidon, 2011; Tenner et al., 2013; Marrocchi et al., 2019a). All these imply that chondrules have formed via reworking of pre-existing solid precursors. Refractory inclusions, e.g., amoeboid olivine aggregates (AOAs) and Ca- and Al-rich inclusions (CAIs), were also present among chondrule precursors (Krot et al., 2004, 2007, 2017; Russell et al., 2005; Nagashima et al., 2015, 2019), but their abundance remains an open topic. Finding out the nature of chondrule precursors is key to track material transport in the accretion disk prior to or at the periods of chondrule formation.

The mass-dependent isotopic variations of Mg can complement the existing chemical and O isotopic observations to trace not only the nature of precursors but also the thermal histories of chondrules, and therefore their formation mechanism. As a moderately refractory element, Mg in silicate melts can be significantly vaporized as Mg or MgO at temperatures above 1800 K under nebular conditions (Floss et al., 1996; Hashimoto, 1990; Davis et al., 1990; Mendybaev et al., 2013). In vacuum this evaporation can be instantaneous at  $> 2173$  K (Hashimoto et al., 1983). While free vaporization can lead to enrichments in the heavier isotopes of Mg (up to 40%/amu in some CAIs), condensation of a Mg-oversaturated gas reservoir can oppositely lead to various scales of enrichments in lighter isotopes of Mg in the condensates relative to the residual gas (Richter, 2004; Simon et al., 2005). This might be the

case for AOAs and some CAIs that have a condensate origin (Krot et al., 2004; Marrocchi et al., 2019b). It is possible that early condensation and evaporation processes in the protosolar nebula have produced distinct mass-dependent Mg isotopic variations in different types of refractory inclusions (e.g., Niederer and Papanastassiou, 1984; Clayton et al., 1988; Simon et al., 2005; Davis et al., 1990; Mendybaev et al., 2013), therefore leaving the fingerprints for discriminating the contribution of these refractory inclusions in chondrules. Moreover, the mass-dependent Mg isotopic fractionations of olivines and mesostases in chondrules can be used to test whether chondrule melts have been subjected to Mg evaporation during the last melting events, which is crucial for deciphering thermal histories of chondrules, i.e., the peak temperatures and the cooling rates. Such evaporation-induced Mg isotopic signatures can be blurred by the effect of olivine dilution when measuring bulk chondrules, therefore calling for an *in situ* high-precision mass-dependent Mg isotopic study.

In addition to the mass-dependent variations of the concentrations of the three Mg stable isotopes ( $^{24}\text{Mg}$ ,  $^{25}\text{Mg}$ ,  $^{26}\text{Mg}$ ), a fraction of radiogenic  $^{26}\text{Mg}$  from the decay of  $^{26}\text{Al}$  ( $T_{1/2} = 0.717$  Myr; Lee et al., 1976) can be added to chondritic components. Before the extinction of  $^{26}\text{Al}$ , the various phases inside either chondrules or refractory inclusions would develop with time various degrees of enrichments in radiogenic  $^{26}\text{Mg}$  that are proportional to the  $^{27}\text{Al}/^{24}\text{Mg}$  ratios, thus forming  $^{26}\text{Al}$ - $^{26}\text{Mg}$  isochrons. Measuring simultaneously the mass-dependent and non mass-dependent Mg isotopic variations of individual phases of chondrules and refractory inclusions in chondrites can be used in theory for resolving the chronology of the thermal processes producing the observed mass-dependent Mg isotopic fractionations (Young et al.,

2002a, 2005; Simon et al., 2005).

Such an *in situ* determination of mass-dependent Mg isotopic fractionation is presently limited. The main *in situ* tool to analyze radiogenic  $^{26}\text{Mg}$  variations, SIMS, cannot provide sufficient precision and accuracy for the mass-dependent Mg isotopic measurements due to the strong matrix effects. For instance, a large set of natural or synthetic olivine and komatiitic, basaltic to andesitic glass standards show 8‰/amu variations caused by matrix effects (Chaussidon et al., 2017), and at fixed MgO contents, minor elements in olivines (e.g.,  $\text{Cr}_2\text{O}_3$ ) can lead to positive biases of 2‰/amu on the measured Mg isotopic compositions (Fukuda et al., 2020; Nagashima et al., 2020). It is also noteworthy that the mesostasis phases in chondrules have been notoriously known for their highly heterogeneous chemical compositions (e.g., Jones and Scott, 1989; Alexander and Grossman, 2005; Libourel et al., 2006; Olsen et al., 2016), making the determination of mass-dependent Mg isotopic variations by SIMS for both olivine/pyroxene and mesostasis phases challenging. To circumvent these limitations of SIMS measurement and to investigate the formation of chondrules, we have developed an *in situ* nanosecond laser ablation multi-collector inductively-coupled-plasma mass-spectrometry (LA-MC-ICP-MS) method to measure with high precision and accuracy simultaneously the  $^{25}\text{Mg}/^{24}\text{Mg}$ ,  $^{26}\text{Mg}/^{24}\text{Mg}$ ,  $^{27}\text{Al}/^{24}\text{Mg}$  and  $^{44}\text{Ca}/^{24}\text{Mg}$  ratios of the major silicate phases of chondrules and refractory inclusions. The results show that matrix-induced Mg isotopic fractionations among various mineral and glass samples can be reduced relative to SIMS by using LA-MC-ICP-MS (1.5-2 ‰/amu variation), which is however still not negligible as suggested earlier (Young et al., 2002a, 2005; Simon et al., 2005). We further



demonstrate that after proper calibration, LA-MC-ICP-MS can likely provide at the same time the  $^{26}\text{Al}$ - $^{26}\text{Mg}$  isochrons and accurate measurements of  $^{25}\text{Mg}/^{24}\text{Mg}$  variations. Two of the studied chondrules were measured by SIMS following a more "classical" *in situ* approach. All these data are used to put new constraints on the nature of precursors and cooling histories of the present chondrules.

## 2. Samples and methods

### 2.1. Mineral and glass standards

Three sets of well-characterized mineral and glass standards were used throughout the development of the techniques for data quality control, including six synthetic olivines (Ol synth Watson #01, #02, #03, #04, #05 and #6) with various MgO contents of 32.83-49.33 wt% (Chaussidon et al., 2017), eleven komatiitic/basaltic/andesitic glasses (StHs6/80-G, BCR-2G, TB-1G, T1-G, ML3B-G, BHVO-2G, KL2-G, MORB-CLDR01RV, BIR-1G, GOR132-G and GOR128-G) (Chaussidon et al., 2017), and four CaO-MgO- $\text{Al}_2\text{O}_3$ - $\text{SiO}_2$  (CMAS) glasses (CMAS-synth-I, -II, -III and -IV). We consider that the komatiitic, basaltic and andesitic glasses, and the CMAS glasses can represent two extreme analogs of refractory inclusions and the mesostasis phases in chondrules. The chemical and Mg isotopic compositions of these standards have been provided in Table 1 with the extended details in Table S1. One diopside and one crystalline MORB have also been included to scrutinize the applicability of the method to the samples with different matrices.

## 2.2. Chondrules and refractory inclusions from Allende and Leoville CV3 chondrites

A thick section of Allende CV3 chondrite was mapped for petrography and chemical compositions by scanning electron microscope (SEM) at the Institut de Physique du Globe de Paris (IPGP) and CRPG-CNRS (Nancy), France. Another Leoville CV3 thick section was characterized by electron microprobe (EMP) at the American Museum of Natural History (AMNH), United States, following the protocol described in Ebel et al. (2016). Three Allende chondrules including one type IA (B-Ch5), one Al-rich (C-Ch1) and one type IIAB (B-Ch1), as well three type IA chondrules from Leoville (Leo-4337-t2-ps2B-c2, Leo-4337-t2-ps2B-c9 and Leo-4337-t2-ps2B-c7) were selected for LA-MC-ICPMS analyses. The diameter of these chondrules typically ranges between 1 mm and 2 mm (Figs. S1 and S2). These chondrules are porphyritic with significant volumes of mesostases, allowing for a determination of the phase relation for Mg isotopes. Also measured in the same sessions were the refractory inclusions, including one Allende melilite sample (Mel-1) that is zoned with an åkermanite-rich core and a gehlenite-rich rim, one Leoville AOA (i.e., Leo-4337-t2-ps2B-aoa1), and three fine-grained CAIs (i.e., Leo-4337-t2-ps2B-ca1, Leo-4337-t2-ps2B-ca3 and Leo-4337-t2-ps2B-ca4) from Leoville (see Fig. S1 and S2 for the compositional maps of these samples).

## 2.3. Laser system and mass spectrometry

In this study, a nanosecond 193 nm ultra-short ATLex 300si excimer laser ablation system was coupled with a Thermo-Scientific Neptune MC-ICP-MS at IPGP for *in situ* LA-MC-ICP-MS Mg isotopic analysis. The typical duration of the laser pulses is around 4 ns. For the

analytical sessions with Allende and Leoville chondrites, sample bracketing with San Carlos olivines (i.e., analysis of San Carlos olivines after each of one or two spots on mineral and glass standards, and the components in chondrites) was used to correct for instrumental fractionation. Duplicate analyses of synthetic olivines and glass standards were conducted over each session to monitor the stability of matrix-induced effects on the measured elemental and Mg isotopic compositions. The washout time was around 10 s after ceasing ablation, and the pause time between two analyses was set to be 60-90 s. Analyses were carried out with a spot size of 40  $\mu\text{m}$ , a repetition rate of 3 Hz, and a gas flow rate of 1.0-1.2 L/min. Each spot contains 400 laser burst shots, and typical ablation depths are 20-25  $\mu\text{m}$ . To investigate the chemistry-controlled matrix effects, laser fluence was fixed in each session to avoid further complication (3.37 J/cm<sup>2</sup> for the Allende session, **Session 1**, and 4.23 J/cm<sup>2</sup> for the Leoville session, **Session 2**) (Table S2), the criteria being that the intensity on  $^{24}\text{Mg}^+$  must be similar ( $\pm 10\%$ ) for olivines with a similar Fo content. On MC-ICP-MS, a medium mass resolution mode ( $M/\Delta M \approx 5000$ ) was used, which theoretically can resolve all the isobaric interferences from  $^{48}\text{Ti}^{2+}$  and  $^{48}\text{Ca}^{2+}$  on  $^{24}\text{Mg}^+$ , and those from  $^{52}\text{Cr}^{2+}$  and  $^{12}\text{C}^{14}\text{N}^+$  on  $^{26}\text{Mg}^+$ . Nonetheless, a dilemma is that the masses of doubly charged ions such as  $^{48}\text{Ti}^{2+}$  and  $^{48}\text{Ca}^{2+}$  are lower than that of  $^{24}\text{Mg}^+$ , whereas the mass of molecular ions  $^{12}\text{C}^{14}\text{N}^+$  is higher than that of  $^{26}\text{Mg}^+$ . Because interferences can only be avoided by making measurements on one flank of the  $^{24}\text{Mg}^+$  or  $^{26}\text{Mg}^+$  peak, it is thus not possible to avoid at the same time  $^{48}\text{Ti}^{2+}$  or  $^{48}\text{Ca}^{2+}$  and  $^{12}\text{C}^{14}\text{N}^+$ . In this study, the priority was to avoid the uncorrectable molecular interference from  $^{12}\text{C}^{14}\text{N}^+$  by measuring the ion intensities at the lower masses of 24, 25 and 26. It was therefore necessary to monitor the intensity of

another doubly charged ion of Ca (e.g.,  $^{44}\text{Ca}^{2+}$ ) to correct for the interference from  $^{48}\text{Ca}^{2+}$  on  $^{24}\text{Mg}^+$ , which also allows a further estimate on the interferences from  $^{48}\text{Ti}^{2+}$  and  $^{52}\text{Cr}^{2+}$  (see below).

To monitor the intensities of the masses 22 to 27, we used a dynamic mode with two cup configurations. The Faraday cup positions and the magnitude of the magnetic field were adjusted to align the  $^{24}\text{Mg}^+$  (L3-F),  $^{25}\text{Mg}^+$  (C-F),  $^{26}\text{Mg}^+$  (H2-F) and  $^{27}\text{Al}^+$  (H4-F) peaks (Table S2), and the measurements were conducted on the left shoulder of the peaks to avoid  $^{12}\text{C}^{14}\text{N}^+$  isobaric interference (main cup configuration). For every five cycles, the central mass was moved from 25 to 23 to monitor simultaneously the intensities of  $^{44}\text{Ca}^{2+}$  (mass 22, L4-F) and  $^{24}\text{Mg}^+$  (mass 24, H2-F). Note that two additional sessions on the mineral and glass standards were carried out with either a large spot size of 110  $\mu\text{m}$  or a high laser fluence of 11.47 J/cm<sup>2</sup> to investigate the potential effects from sample loading or sample melting.

#### 2.4. Data reduction and notation

Each laser spot contains 18-19 cycles for the main cup configuration and 4-5 cycles for the sub cup configuration. Data reduction was implemented through integrating these cycles except for the transient cycles at the beginning or the end of ablation (intensity varying more than 25% from the plateau intensity). The background of each ablation spot was subtracted with a polynomial fit to the background cycles. The Mg isotopic compositions and variations observed in this study are given in per mil notation that can be defined as:

$$\delta^i\text{Mg}(\text{‰}) = \left[ \frac{\left( {}^i\text{Mg} / {}^{24}\text{Mg} \right)_{\text{sample}}}{\left( {}^i\text{Mg} / {}^{24}\text{Mg} \right)_{\text{DSM-3}}} - 1 \right] \times 1000 \quad (1)$$

where  ${}^i\text{Mg}$  represents  ${}^{25}\text{Mg}$  or  ${}^{26}\text{Mg}$ , and  $\delta^i\text{Mg}$  stands for the isotopic difference in per mil relative to the Dead Sea magnesium (DSM-3) standard (Galy et al., 2003). The mass-independent or non-mass dependent Mg isotopic fractionations ( $\Delta^{26}\text{Mg}$ ) can then be provided as:

$$\Delta^{26}\text{Mg} = \delta^{26}\text{Mg} - \frac{\delta^{25}\text{Mg}}{\beta_{\text{nat}}} \quad (2)$$

where  $\beta_{\text{nat}}$  represents a chosen mass fractionation law for Mg isotopic variations in the natural samples. The  $\Delta^{26}\text{Mg}$  value has been usually referred to as  $\delta^{26}\text{Mg}^*$  in the case of radiogenic  ${}^{26}\text{Mg}$  excesses or depletions in meteorite samples. Throughout this study, we adopt a  $\beta$  value of 0.517 for both Mg isotopic fractionations in natural samples and those caused by matrix effects, which is in between the kinetic and equilibrium mass fractionation laws, and is close to a Rayleigh process (Young et al., 2002b; Davis et al., 2015).

## 2.5. SIMS measurements

After LA-MC-ICP-MS measurements, the Allende thick section was cut with diamond wire and mounted into epoxy, and polished to remove the laser ablation pits and gain a new pristine surface for SIMS measurements. Magnesium isotopes and  ${}^{27}\text{Al}/{}^{24}\text{Mg}$  ratios of two Allende chondrules (i.e., B-Ch5 and C-Ch1) were measured with a CAMECA large radius ims 1280HR2 secondary ion mass spectrometry (SIMS) housed at CRPG-CNRS (Nancy). Measurements were conducted following the protocols described in Villeneuve et al. (2009)

and Luu et al. (2013) except that a Hyperion ion source was used. A primary  $O^-$  ion beam of 25 nA  $O^-$  was accelerated at 13 kV and focused to achieve spots of 8-10  $\mu m$  diameter. The secondary ions of Al and Mg isotopes were measured under multi-collection mode (L'2, C, H1 and H'2 for  $^{24}Mg^+$ ,  $^{25}Mg^+$ ,  $^{26}Mg^+$  and  $^{27}Al^+$ , respectively) at a mass resolving power of  $\approx 2500$ . To minimize the isobaric interference of  $^{24}MgH^+$  on  $^{25}Mg^+$ , the vacuum was kept below  $4 \times 10^{-9}$  torr in the sample chamber. During the analytical sessions, San Carlos olivine and basaltic glass standards were used to correct for matrix effects on the Al/Mg yield for silicates. The analytical uncertainties on the measured Mg isotopic results (with 2SD values of  $\pm 0.06$ - $0.10\%$  for  $\delta^{26}Mg^*$  values on Mg-rich olivines) and  $^{27}Al/^{24}Mg$  ratios ( $\pm 7\%$ , 2SD) were estimated by considering both counting statistics and uncertainties on standards. Arising from the strong and complicated matrix effects (Chaussidon et al., 2017; Fukuda et al., 2020; Nagashima et al., 2020), measuring precisely and accurately the  $\delta^{25}Mg$  values by SIMS for chondrules requires a strict calibration of the matrix-induced Mg isotopic effects with a large set of standard materials of various matrices, which is beyond the scope of this study.

### 3. LA-MC-ICP-MS method for Mg isotopic measurements

#### 3.1. Doubly charged ion interferences on Mg isotopes

Arising from the high energy input in the ICP sources (particularly for dry plasma setting by LA-MC-ICP-MS measurements; Janney et al., 2011), various types of doubly charged ions, such as  $^{48}Ca^{2+}$  and  $^{48}Ti^{2+}$  on  $^{24}Mg^+$ , and  $^{52}Cr^{2+}$  on  $^{26}Mg^+$ , can be produced and create mass interferences with the ions of Mg isotopes. It is therefore necessary to quantify the production

of these doubly-charged ions during the measurements. This can be approached using three types of mineral and glass standards (Table 1 and S1) covering the compositional range of meteoritic samples, and having various CaO, TiO<sub>2</sub> and Cr<sub>2</sub>O<sub>3</sub> contents: synthetic olivines (devoid of CaO, TiO<sub>2</sub> and Cr<sub>2</sub>O<sub>3</sub>), komatiitic, basaltic and andesitic glasses (with various amounts of CaO, TiO<sub>2</sub> and Cr<sub>2</sub>O<sub>3</sub>), and CaO-MgO-Al<sub>2</sub>O<sub>3</sub>-SiO<sub>2</sub> (CMAS) glasses having only CaO. All these standards are terrestrial or synthesized from terrestrial materials, so that they contain no radiogenic <sup>26</sup>Mg excess and form a baseline to detect the interferences resulting in apparent non-mass dependent effects on the measured Mg isotopic ratios. This provides a way to scrutinize the reliability of the protocol chosen for interference correction.

As addressed above, Mg isotopic measurements on the lower flanks of the 24, 25 and 26 peaks are subjected to isobaric interferences from doubly charged ions of Ca, Ti and Cr. As such, the measured Mg isotopic ratios would be biased as following:

$$\left( \frac{{}^{25}\text{Mg}}{{}^{24}\text{Mg}} \right)_{\text{meas}} = \frac{{}^{25}\text{Mg}^+}{{}^{24}\text{Mg}^+ + {}^{48}\text{Ca}^{2+} + {}^{48}\text{Ti}^{2+}} \quad (3)$$

$$\left( \frac{{}^{26}\text{Mg}}{{}^{24}\text{Mg}} \right)_{\text{meas}} = \frac{{}^{26}\text{Mg}^+ + {}^{52}\text{Cr}^{2+}}{{}^{24}\text{Mg}^+ + {}^{48}\text{Ca}^{2+} + {}^{48}\text{Ti}^{2+}} \quad (4)$$

As the <sup>44</sup>Ca<sup>2+</sup> signals have been monitored, the <sup>48</sup>Ca<sup>2+</sup>/<sup>24</sup>Mg<sup>+</sup> ratios of samples can be written:

$$\frac{{}^{48}\text{Ca}^{2+}}{{}^{24}\text{Mg}^+} = \frac{{}^{44}\text{Ca}^{2+}}{{}^{24}\text{Mg}^+} \times \frac{{}^{48}\text{Ca}^{2+}}{{}^{44}\text{Ca}^{2+}} \quad (5)$$

The apparent non-mass dependent Mg isotopic effects from doubly charged ion interferences of Ca, Ti and Cr (noted hereafter  $\Delta^{26}\text{Mg}_{\text{Ca+Ti+Cr}}$ ) should follow a linear relation against the measured <sup>44</sup>Ca<sup>2+</sup>/<sup>24</sup>Mg<sup>+</sup> ratio (see equations A1 to A11 in **Appendix** for demonstration):

$$\Delta^{26}\text{Mg}_{\text{Ca+Ti+Cr}} \approx \left( 0.934 \times \frac{{}^{44}\text{Ca}^{2+}}{{}^{24}\text{Mg}^{+}} \times \frac{{}^{48}\text{Ca}^{2+}}{{}^{44}\text{Ca}^{2+}} + 0.934 \times \frac{{}^{48}\text{Ti}^{2+}}{{}^{24}\text{Mg}^{+}} + \frac{{}^{52}\text{Cr}^{2+}}{{}^{26}\text{Mg}^{+}} \right) \times 10^3 \quad (6)$$

In this study, the intensities of  ${}^{48}\text{Ti}^{2+}$  and  ${}^{52}\text{Cr}^{2+}$  were not measured directly. Nonetheless, the production of these two doubly charged ions can be quantified by comparing  $\Delta^{26}\text{Mg}_{\text{Ca+Ti+Cr}}$  with the measured  ${}^{44}\text{Ca}^{2+}/{}^{24}\text{Mg}^{+}$  ratios (equation 6 and Fig. 1). The results from the present mineral and glass standards show that the  $\Delta^{26}\text{Mg}_{\text{Ca+Ti+Cr}}$  values always define nice linear correlations against the measured  ${}^{44}\text{Ca}^{2+}/{}^{24}\text{Mg}^{+}$  ratios with intercepts that are very close to zero (Fig. 1). Considering that the various mineral and glass standards have distinct CaO,  $\text{TiO}_2$  and  $\text{Cr}_2\text{O}_3$  contents, the linear correlations can support that the doubly charged ion interferences on Mg isotopes in the MC-ICP-MS are predominantly  ${}^{48}\text{Ca}^{2+}$  with very few  ${}^{48}\text{Ti}^{2+}$  and  ${}^{52}\text{Cr}^{2+}$ . Assuming that the singly charged ionization rate of Mg is close to unity and  ${}^{48}\text{Ca}^{2+}$ ,  ${}^{48}\text{Ti}^{2+}$  and  ${}^{52}\text{Cr}^{2+}$  ions have the same transmission rate as  ${}^{24}\text{Mg}^{+}$  ions in the MC-ICP-MS, the doubly charged ionization rate of Ca in the ICP source (i.e., the production rate of  $\text{Ca}^{2+}$ ) should vary between 16% and 24% between different sessions based on the correlations in Fig. 2. According to the correlations in Fig. 1, the instrumental  ${}^{48}\text{Ca}^{2+}/{}^{44}\text{Ca}^{2+}$  ratio within each analytical session can be determined with an uncertainty better than  $\pm 5\%$ , thus allowing a sufficient correction of  ${}^{48}\text{Ca}^{2+}$  interferences on  ${}^{24}\text{Mg}^{+}$  using equation 3 to 5. After correction of  ${}^{48}\text{Ca}^{2+}$  interferences, even the basaltic glass standard with the highest  ${}^{48}\text{Ti}/{}^{24}\text{Mg}$  ratio of 0.2955 (BCR-2G) turns out to have an apparent non-mass dependent Mg isotopic effect ( $\Delta^{26}\text{Mg}$ ) within  $\pm 0.05\%$  identical to those for synthetic Ti-free CMAS glasses (Tables S5 and S6). This suggests that the production rate of doubly charged Ti and Cr ions, in total, should be  $\leq 0.02\%$ , and that the present measurements of non-mass dependent Mg isotopic variations in natural



samples with  $^{48}\text{Ti}/^{24}\text{Mg}$  ratios  $\leq 0.3$  by LA-MC-ICP-MS were not significantly affected by  $^{48}\text{Ti}^{2+}$  and  $^{52}\text{Cr}^{2+}$  interferences.

### 3.2. Matrix effects for mass-dependent Mg isotopic measurements

After correction of  $^{48}\text{Ca}^{2+}$  interferences, the measured Mg isotopic compositions of the standards may differ from their true isotopic compositions, as the result of matrix effects (i.e. different chemistry between samples and the bracketing standard). It is notable that such matrix-caused Mg isotopic fractionations ( $[\delta^{25}\text{Mg}_{\text{measured}} - \delta^{25}\text{Mg}_{\text{true}}]$ ) on the mineral and glass standards (excluding the CMAS glasses) are negatively correlated with the Mg Intensity Normalized to the Bracketing Standard (MINBS) in a linear or polynomial manner (Fig. 3):

$$[\delta^{25}\text{Mg}_{\text{measured}} - \delta^{25}\text{Mg}_{\text{true}}] = a + b \times (\text{MINBS}) + c \times (\text{MINBS})^2 \quad (7)$$

The MINBS values here reflect, to first order, the MgO contents of the samples, relative to that of the bracketing standard. This suggests that, at least for olivine, pyroxene and komatiitic/basaltic/andesitic glasses, matrix-induced Mg isotopic effects by LA-MC-ICP-MS are mainly controlled by the differences in major element abundances. A similar systematics for matrix-induced isotopic effects has also been observed in the case of Mg and Fe isotopic analyses of olivines by LA-MC-ICP-MS in Sio et al. (2013). Since the systematics can vary between sessions, calibration is required for each analytical session. Using these empirical calibrations, a correction can be carried out to eliminate Mg isotopic fractionations induced by matrix effects.

### 3.3. Effects from ablation spot size and laser fluence for CMAS-like samples

It is noteworthy that using a large spot size of 110  $\mu\text{m}$ , the CMAS glass standards form different calibrations for  $^{44}\text{Ca}/^{24}\text{Mg}$  and  $^{27}\text{Al}/^{24}\text{Mg}$  ratio measurements from those of olivine and komatiitic/basaltic/andesitic glass standards (Fig. 2). We speculate that loading large amounts of sample (i.e. in case of large spot size) may have led to inconsistent ionization rates or inconsistent ion transmission rates for Mg, Al and Ca between standards of different matrices, even within the same analytical session. This calls for cautions to match the matrices between standards and natural samples when using LA-MC-ICP-MS to investigate the  $^{26}\text{Al}$ - $^{26}\text{Mg}$  system in meteorites. In detail, with a large spot size of  $\geq 100 \mu\text{m}$ , the calibration line defined for  $^{27}\text{Al}/^{24}\text{Mg}$  ratio measurements from olivines, and komatiitic to andesitic glass standards cannot be used for CMAS-like samples (e.g., some CAI samples). In fact, it could lead to lower the  $^{27}\text{Al}/^{24}\text{Mg}$  ratios, which would result in higher initial  $^{26}\text{Al}/^{27}\text{Al}$  ratios and thus biased  $^{26}\text{Al}$ - $^{26}\text{Mg}$  isochrons.

We also figure out that the matrix-induced Mg isotopic fractionations on CMAS glasses are quite sensitive to the choice of laser fluence for ablation. Compared to the systematics defined from olivines, komatiitic to andesitic glasses, diopside and crystalline MORB, the measurements of CMAS glasses yield lower  $[\delta^{25}\text{Mg}_{\text{measured}} - \delta^{25}\text{Mg}_{\text{true}}]$  values at a low laser fluence of 3.37 or 4.23  $\text{J}/\text{cm}^2$ , and higher  $[\delta^{25}\text{Mg}_{\text{measured}} - \delta^{25}\text{Mg}_{\text{true}}]$  values at a high laser fluence of 11.47  $\text{J}/\text{cm}^2$  (Fig. 3B). Such different matrix-induced Mg isotopic fractionations are likely due to the inconsistent melting behaviors of the CMAS glasses relative to other standards during their interaction with the nanosecond laser pulses, which can likely produce aerosols

with distinct particle size distribution and therefore complicate ionization behaviors in the ICP source. This is likely corroborated by the significant changes in Mg ion intensity for the CMAS glasses relative to other komatiitic to andesitic glass standards at varying laser fluences (Fig. 3B). One may expect to identify an optimal laser fluence for a nanosecond laser system to minimize the matrix effects on the measured  $\delta^{25}\text{Mg}$  values for the samples of different matrices. However, potential inconsistent melting behavior between standards and samples at various laser settings remains a major issue when using a nanosecond laser ablation system to measure *in situ* mass-dependent Mg isotopic fractionations. This can possibly be overcome by applying a femtosecond laser ablation system, which provides much shorter laser pulses and may avoid melting of samples.

#### 3.4. Applicability of the olivine and komatiitic/basaltic/andesitic glass standards to correct for matrix-induced Mg isotopic fractionations on chondrule phases

The mesostasis phases in chondrules are notoriously known for the complicated chemical compositions, and it is thus unrealistic to prepare standards matching exactly the matrices. However, there have been hints that the mesostases in chondrules of carbonaceous chondrites (Vigarano, NWA 3118 and NWA 6043) have chemical compositions ranging from komatiitic, basaltic to andesitic, with  $\text{SiO}_2$  contents of 43.49-56.34 wt% and MgO contents of 2.26-20.96 wt% (Olsen et al., 2016). These compositions have been well encompassed by the komatiitic, basaltic and andesitic glasses in this study ( $\text{SiO}_2$  = 45.50-63.70 wt% and MgO = 1.97-26.00 wt%; Table 1). Along with the Mg isotopic compositions, our LA-MC-ICP-MS technique is

able to obtain the  $^{27}\text{Al}/^{24}\text{Mg}$  and  $^{44}\text{Ca}/^{24}\text{Mg}$  ratios for the same ablation spots (Fig. 2), which further show that the used olivine and komatiitic to andesitic glass standards can serve as nice analogs for the measured chondrules phases in Allende and Leoville chondrites (Fig. 4). As such, we consider that the matrix-induced Mg isotopic fractionations on the chondrule phases by LA-MC-ICP-MS can be sufficiently tracked via measurements of olivine and komatiitic to andesitic glass standards within the same analytical session.

It is noteworthy that the Allende melilite phases are characterized by the  $^{27}\text{Al}/^{24}\text{Mg}$  and  $^{44}\text{Ca}/^{24}\text{Mg}$  ratios distinct from those of the komatiitic/basaltic/andesitic glasses but similar to those of the CMAS glasses (Fig. 4), which can at least partially account for the inconsistent matrix-induced Mg isotopic effects on the CMAS glasses relative to the other mineral and glass standards (Fig. 3B). For the data from the Allende and Leoville sessions, we adopted the calibration from olivine and komatiitic/basaltic/andesitic glass standards to correct for the matrix-induced Mg isotopic fractionations on the various phases of the studied chondrules. Considering that the Allende and Leoville sessions were with low laser fluences of 3.37 or 4.23 J/cm<sup>2</sup>, such a protocol of matrix effect correction may biasedly lead to sub per mil lower  $\delta^{25}\text{Mg}$  values for the melilite phases in Allende, and possibly also other refractory inclusions if their compositions have evolved partly to the CMAS compositions.

### 3.5. Error estimate for the measured Mg isotopic results

For the Mg isotopic measurements from LA-MC-ICP-MS measurements, three sources of analytical uncertainty have to be considered: (i) internal uncertainty of the measurements, (ii)

uncertainty from  $^{48}\text{Ca}^{2+}$  interference correction and (iii) uncertainty from matrix effect correction. Each laser ablation spot on a sample forms an individual analysis. The internal uncertainty can be estimated using duplicate analyses of mineral and glass standards. For the Allende and Leoville sessions, the internal uncertainties are related to the number of Mg ions detected and can be assessed from the 2SD of the delta values of the raw Mg isotopic ratios of olivine and glass standards. The uncertainty from  $^{48}\text{Ca}^{2+}$  correction is controlled by the measured  $^{44}\text{Ca}^{2+}/^{24}\text{Mg}^+$  ratios and the uncertainty on the estimated  $^{48}\text{Ca}^{2+}/^{44}\text{Ca}^{2+}$  ratios. The additional uncertainty from matrix effect correction can be estimated from fitting the  $[\delta^{25}\text{Mg}_{\text{measured}} - \delta^{25}\text{Mg}_{\text{true}}]$  values and MINBS values in each session following equation 7. Note that an additional uncertainty on the  $\delta^{26}\text{Mg}^*$  values due to matrix effect correction can arise from the choice of  $\beta_{\text{mtr}}$ , which can range between 0.511 for kinetic fractionation law and 0.521 for equilibrium fractionation law (Young et al., 2002b; Davis et al., 2015). However, this effect should be negligible at an analytical precision of  $\pm 0.04\text{‰}$  on  $\delta^{26}\text{Mg}^*$ . The final uncertainties of the  $\delta^{25}\text{Mg}$ ,  $\delta^{26}\text{Mg}$  and  $\delta^{26}\text{Mg}^*$  values can be obtained as the sums of the uncertainties from these different sources.

After error propagation, the 2SD uncertainties on  $\delta^{26}\text{Mg}^*$  are  $\pm 0.04\text{-}0.06\text{‰}$  for olivines and  $\pm 0.10\text{-}0.60\text{‰}$  for mesostasis and melilite phases. For  $\delta^{25}\text{Mg}$ , the 2SD uncertainties are  $\pm 0.25\text{-}0.30\text{‰}$  for olivines whereas  $\pm 0.30\text{-}0.55\text{‰}$  for mesostasis and melilite phases. Note that the larger uncertainty on mesostasis and melilite phases than on olivines is due to their lower MgO contents and less Mg ion counts at a fixed laser ablation setting. It is noteworthy that if aiming to measure precisely the  $\delta^{26}\text{Mg}^*$  values of olivine phases in natural samples, San Carlos

olivines or other olivines should be used as the bracketing standards instead of basaltic glasses to reduce as much as possible the uncertainty from sample-to-standard normalization.

### 3.6. Measurements of $\delta^{26}\text{Mg}^*$ and $\delta^{25}\text{Mg}$ values for standards after correction

After correction for  $^{48}\text{Ca}^{2+}$  interferences, all the present mineral and glass standards show  $\delta^{26}\text{Mg}^* \approx 0$  whatever their  $^{27}\text{Al}/^{24}\text{Mg}$  ratios, consistent with the fact that terrestrial samples have no radiogenic  $^{26}\text{Mg}$  excesses (Fig. 5). Using the same interference correction protocol, the crystalline MORB provides a  $\delta^{26}\text{Mg}^*$  value of  $-0.02 \pm 0.06\text{‰}$  (2SE,  $n = 10$ ), confirming that the method also works for crystalline samples. For the measurements of  $\delta^{25}\text{Mg}$  values, the olivines and komatiitic to andesitic glass standards all provide  $\delta^{25}\text{Mg}$  values identical within uncertainty to the  $\delta^{25}\text{Mg}$  values from solution MC-ICP-MS measurements (Fig. 6). However, using the calibration from olivine and komatiitic/basaltic/andesitic glass standards to correct for matrix effects would artificially produce lower  $\delta^{25}\text{Mg}$  values for CMAS glasses at low laser fluence, but higher  $\delta^{25}\text{Mg}$  values at high laser fluence (Fig. 6).

## 4. Results

### 4.1. $\delta^{26}\text{Mg}^*$ results

The Allende melilite grain, and the Leoville AOA and CAI samples are characterized by significant enrichments in  $^{26}\text{Mg}$  relative to terrestrial standards, i.e. positive  $\delta^{26}\text{Mg}^*$  values, forming well-defined  $^{26}\text{Al}$ - $^{26}\text{Mg}$  isochrons (Fig. 7A-C) yielding  $(^{26}\text{Al}/^{27}\text{Al})_{\text{initial}}$  ratios from  $5.46 (\pm 0.38) \times 10^{-5}$  to  $6.14 (\pm 0.92) \times 10^{-5}$  according to:

$$\delta^{26}\text{Mg}^* \approx (\delta^{26}\text{Mg}^*)_{\text{initial}} + 1000 \times \left[ \left( \frac{^{26}\text{Al}}{^{27}\text{Al}} \right)_{\text{initial}} \times \left( \frac{^{27}\text{Al}}{^{24}\text{Mg}} \right)_{\text{sample}} \right] / 0.13932 \quad (8)$$

where 0.13932 is the reference  $^{26}\text{Mg}/^{24}\text{Mg}$  ratio from Catanzaro et al. (1966). These initial  $^{26}\text{Al}/^{27}\text{Al}$  ratios are consistent with the previous data for refractory inclusions, which were measured by thermal ionization mass spectrometry (TIMS), SIMS, MC-ICP-MS or LA-MC-ICP-MS (Lee et al., 1976; Bizzarro et al., 2004; Young et al., 2005; Simon et al., 2005; Jacobsen et al., 2008; Larsen et al., 2011; Wasserburg et al., 2012; Kita et al., 2012; Mishra and Chaussidon, 2014). For Allende chondrule C-Ch1, the LA-MC-ICP-MS and SIMS data align along a single isochron which, together with the results of AOA and CAIs, support the robustness of the LA-MC-ICP-MS method to monitor radiogenic  $^{26}\text{Mg}$  in meteorites.

Compared to refractory inclusions, the present chondrules show smaller but resolvable  $^{26}\text{Mg}$  excesses, with  $^{26}\text{Al}$ - $^{26}\text{Mg}$  isochrons having  $(^{26}\text{Al}/^{27}\text{Al})_{\text{initial}}$  ratios from  $0.16 (\pm 0.08) \times 10^{-5}$  to  $1.87 (\pm 0.92) \times 10^{-5}$  (Fig. 7D-H). These  $(^{26}\text{Al}/^{27}\text{Al})_{\text{initial}}$  ratios are within uncertainty identical to those published for chondrules from carbonaceous and ordinary chondrites (e.g., Kita et al., 2000; Luu et al., 2015; Villeneuve et al., 2009), and would correspond to ages of  $1.06^{+0.70}_{-0.41}$  to  $3.6^{+0.7}_{-0.4}$  Myr after CAIs, assuming homogenous  $^{26}\text{Al}/^{27}\text{Al}$  as a function of time in the early Solar System. Note that the low initial  $^{26}\text{Al}/^{27}\text{Al}$  ratio of  $0.16 (\pm 0.08) \times 10^{-5}$  for the Allende B-CH5 chondrule is likely due to the fact that the linear regression is controlled by the plagioclase grains that are not the major Mg-bearing phases in the mesostases but have very high  $^{27}\text{Al}/^{24}\text{Mg}$  ratios of 22.98-51.78 and are thus easily disturbed for Mg isotopes (Fig. 7D). Including only the data from Mg-rich phases returns to a higher initial  $^{26}\text{Al}/^{27}\text{Al}$  ratio of 1.85  $(\pm 1.02) \times 10^{-5}$  for the Allende B-CH5 chondrule. In the Leoville chondrule Leo-4337-t2-psB-

c7, two Ca-rich pyroxenes and several olivines plot close to the bulk CAI  $^{26}\text{Al}$ - $^{26}\text{Mg}$  isochron (Jacobsen et al., 2008; Larsen et al., 2011), while the other olivines, Ca-poor pyroxenes and mesostases form an isochron giving a much lower initial  $^{26}\text{Al}/^{27}\text{Al}$  ratio of  $\approx 0.8 \times 10^{-5}$  (Fig. 7I).

#### 4.2. $\delta^{25}\text{Mg}$ results

Within the Allende and Leoville chondrules, the Mg-rich olivines show heterogeneous  $\delta^{25}\text{Mg}$  values from  $-1.22 \pm 0.24\text{‰}$  to  $-0.05 \pm 0.24\text{‰}$ , with two out of four type I chondrules (B-Ch5 and Leo-4337-t2-ps2B-c9) containing olivines with  $\delta^{25}\text{Mg}$  values as low as  $-1.22 \pm 0.24\text{‰}$  (Fig. 8). In chondrules B-Ch1, Leo-4337-t2-ps2B-c2 and Leo-4337-t2-ps2B-c7, the olivines have  $\delta^{25}\text{Mg}$  values identical within uncertainty to the glassy mesostases or the clinopyroxene and plagioclase (Fig. 8), while, for the other three chondrules (B-Ch5, C-Ch1 and Leo-4337-t2-ps2b-c9), the glassy mesostases or the clinopyroxene and plagioclase are in average 0.68-0.94‰ higher in  $\delta^{25}\text{Mg}$  relative to the olivines (Fig. 8). These inter-phase differences are robust since, as explained in Section 3.4, the used olivines and komatiitic to andesitic glasses resemble to the measured chondrule phases in chemical composition and are able to serve as standards to correct for matrix effects for the measurements on chondrules. Note that previous SIMS data in chondrules from the Acfer 094 C3 chondrite showed that their olivines, at variance with the present results for Allende and Leoville, have high  $\delta^{25}\text{Mg}$  values up to +1-2‰ (Ushikubo et al., 2013). Nonetheless, these high  $\delta^{25}\text{Mg}$  values in chondrule olivines in Ushikubo et al. (2013) have recently been suggested by Fukuda et al. (2020) to be,



most probably, the results of an incomplete correction of SIMS matrix effects due to minor elements in olivines, which can be up to +2‰/amu for Cr<sub>2</sub>O<sub>3</sub> contents of 0.8 wt.%. We stress that reliable "bulk"  $\delta^{25}\text{Mg}$  values cannot be obtained by averaging the LA-MC-ICP-MS data since most of the ablation spots in olivines have been located in the olivine-core areas to avoid ablation of mesostasis phases.

The most negative  $\delta^{25}\text{Mg}$  values in the Leoville AOA are in the olivines (from  $-1.63 \pm 0.24\text{‰}$  to  $-1.12 \pm 0.25\text{‰}$ ), while more variable  $\delta^{25}\text{Mg}$  values ( $-1.40 \pm 0.28\text{‰}$  to  $-0.03 \pm 0.25\text{‰}$ ) are present in other Al- and Ca-rich phases (Fig. 8). Such low  $\delta^{25}\text{Mg}$  values in AOAs are consistent with previous data by solution MC-ICP-MS for AOAs from the CV chondrite Efremovka (Larsen et al., 2011), with 7 out of 8 for these olivines having bulk  $\delta^{25}\text{Mg}$  values from  $-2.465 \pm 0.009\text{‰}$  to  $-1.148 \pm 0.018\text{‰}$  (Fig. 8), as well as the results of olivines in the AOAs from Kaba (CV3.1) and DOM 08006 (CO3.1) carbonaceous chondrites ( $\delta^{25}\text{Mg}$  of  $-3.8 \pm 0.5\text{‰}$  to  $-0.2 \pm 0.3\text{‰}$ ; Fukuda et al., 2021). The fine-grained CAI samples from Leoville exhibit both negative and positive  $\delta^{25}\text{Mg}$  values from  $-1.12 \pm 0.28\text{‰}$  to  $+0.35 \pm 0.32\text{‰}$ . In contrast to the AOA and the fine-grained CAIs in Leoville, the melilite sample in Allende is showing positive and highly varying  $\delta^{25}\text{Mg}$  values of  $+1.32 \pm 0.45\text{‰}$  to  $+8.38 \pm 0.38\text{‰}$ . These positive  $\delta^{25}\text{Mg}$  values are consistent with the commonly observed enrichment in heavy Mg isotopes in type B CAIs due to partial evaporation processes (e.g., Lee and Papanastassiou, 1974; Lee et al., 1976; Clayton et al., 1988; Davis et al., 1990; Mendybaev et al., 2013; Simon et al., 2005). Nonetheless, considering the complicated matrix-induced Mg isotopic fractionations by LA-MC-ICP-MS for the CMAS glass standards, a part of the  $\delta^{25}\text{Mg}$

variations (up to 2.5‰/amu effects; Fig. 3B) in the studied CAI samples with CMAS-like compositions may have come from the insufficient correction of matrix effects, and examination by solution MC-ICP-MS method would be necessary before speaking on their implications for CAI formation.

The range of  $\delta^{25}\text{Mg}$  variations in chondrules by LA-MC-ICP-MS, overall, are consistent with previous data for bulk chondrules by solution MC-ICP-MS (variations up to 1.5‰/amu; Fig. 8; Galy et al., 2000; Bizzarro et al., 2004; Bouvier et al., 2013; Luu et al., 2015; Olsen et al., 2016; van Kooten et al., 2016; Chen et al., 2018). However, the present *in situ* data show that there are Mg-rich olivines in chondrules that trend to  $\delta^{25}\text{Mg}$  values as low as those in AOAs reported here and in Larsen et al. (2011) (Fig. 8).

## 5. Discussion

### 5.1. Super-cooling gas condensates among chondrule precursors

An important result from the LA-MC-ICP-MS study is that two of the four studied type I chondrules have Mg-rich olivines with low  $\delta^{25}\text{Mg}$  values between  $-1.22 \pm 0.24\text{‰}$  and  $-1.00 \pm 0.29\text{‰}$  (10 ablation spots) that are overlapping with the  $\delta^{25}\text{Mg}$  range of the Leoville and Efremovka AOAs (Fig. 8). There is a wealth of *in situ* SIMS O isotopic studies showing the presence (often in type I chondrules of carbonaceous chondrites) of relict olivines formed in the nebular reservoirs (or from precursors) that were more enriched in  $^{16}\text{O}$  than the ambient gases where the last chondrule melting events took place (e.g., Weinbruch et al., 1993; Jones et al., 2004; Pack et al., 2004; Chaussidon et al., 2008; Rudraswami et al., 2011; Libourel and

Chaussidon, 2011; Tenner et al., 2013; Marrocchi et al., 2019a). Nonetheless, these  $^{16}\text{O}$  enrichments are generally much smaller than those in AOAs (Clayton, 1993; Yurimoto et al., 2008; and references therein) except in rare cases (Marrocchi et al., 2019a). Thus, the present  $\delta^{25}\text{Mg}$  similarity between some chondrule olivines and AOAs does not mean necessarily that the precursors of chondrules formed in the same nebular reservoirs than AOAs, but could instead suggest a formation from a similar rapid-cooling condensation process.

For a cooling gas reservoir, kinetic Mg isotopic effects can arise when Mg oversaturation ( $P_{\text{Mg}} \geq P_{\text{Mg,sat}}$ ) occurs due to cooling taking place faster than condensation (Richter, 2004). The isotope fractionation factors on  $^{25}\text{Mg}/^{24}\text{Mg}$  ratio for the condensates are related to the degree of oversaturation (Richter, 2004), which can be approximated as:

$$\alpha_{\text{cond}}^{25/24} \approx 1 + \left( \sqrt{\frac{m_{^{24}\text{Mg}}}{m_{^{25}\text{Mg}}}} - 1 \right) \times \left( 1 - \frac{P_{\text{Mg,sat}}}{P_{\text{Mg}}} \right) \quad (9)$$

where  $m$  represents the atomic mass of isotope  $^{24}\text{Mg}$  or  $^{25}\text{Mg}$ . As such, the  $\delta^{25}\text{Mg}$  values of the instant condensates would be:

$$\delta^{25}\text{Mg}_{\text{cond}} = \delta^{25}\text{Mg}_{\text{gas}} + 1000 \times (\alpha_{\text{cond}}^{25/24} - 1) \quad (10)$$

For a gas reservoir with a chondritic Mg isotopic composition ( $\delta^{25}\text{Mg} = -0.15 \pm 0.04\text{‰}$ , 2SD,  $n = 38$ ; Teng et al., 2010), an equilibrium condensation at slow cooling ( $P_{\text{Mg}} = P_{\text{Mg,sat}}$ ) would exhibit no kinetic effect. While currently there are no data in the literature on the equilibrium Mg isotopic fractionation between solids and gases, we temporarily assume that such effects are negligible, i.e., the  $\delta^{25}\text{Mg}$  value of condensates from equilibrium condensation should be  $-0.15\text{‰}$ . However, a condensation during fast cooling would lead to various degrees of kinetic

Mg isotopic effects depending on  $P_{\text{Mg,sat}}/P_{\text{Mg}}$ . Note that  $\alpha_{\text{cond}}^{25/24}$  can approach  $\sqrt{24/25}$  when the cooling is extremely fast relative to the condensation timescale (in other words,  $P_{\text{Mg}} \gg P_{\text{Mg,sat}}$ ). As modeled in Richter (2004), non-equilibrium condensation at  $\varepsilon = 0.01$  (with  $\varepsilon$  a parameter comparing the condensation timescale relative to the cooling timescale,  $\varepsilon \geq 0.1$  implies fast cooling and  $\varepsilon \ll 1$  slow cooling) can lead to  $\delta^{25}\text{Mg}$  values in the accumulated condensates at 1250 K 2‰ lower than in the initial gas.

Thus, the low  $\delta^{25}\text{Mg}$  values in the olivines of the present chondrules and AOAs likely suggest a rapid-cooling condensation process ( $P_{\text{Mg}} > P_{\text{Mg,sat}}$ ) for the formation of chondrule precursors and AOAs. Such short timescales for condensation of AOAs' olivines have also been proposed on the basis of their light Si isotopic compositions (Marrocchi et al., 2019b). The occurrences of rapid-cooling condensation in multiple nebular regions suggest that super-cooling of gases may be common across the early solar nebula.

## 5.2. Potential Mg isotopic disequilibrium between olivines and mesostases in chondrules

The LA-MC-ICP-MS results from this study show that in some chondrules, olivines and mesostases have significantly heterogeneous  $\delta^{25}\text{Mg}$  values, with the glassy mesostases or the clinopyroxene and plagioclase having  $\delta^{25}\text{Mg}$  values higher than those of olivines (Fig. 8). Such inter-phase  $\delta^{25}\text{Mg}$  differences in chondrules observed by LA-MC-ICP-MS technique can be further scrutinized in the future via either solution MC-ICP-MS method after careful micro-scale sampling or femtosecond laser ablation MC-ICP-MS method.

Carbonaceous chondrites have experienced some degrees of late aqueous alteration in the parent bodies and hydration of the mesostases (e.g., Clayton and Mayeda, 1999). Nonetheless, this late aqueous alteration is unlikely to affect much the Mg isotopic compositions from chondrule formation. (i) Refractory inclusions and chondrules from the same sample sections show no significant disturbance in their  $^{26}\text{Al}$ - $^{26}\text{Mg}$  isochrons, suggesting that the  $^{27}\text{Al}/^{24}\text{Mg}$  variations in the studied chondrules are likely inherited from the melting events prior to  $^{26}\text{Al}$  extinction, implying that the mobility of Mg by aqueous alteration has been weak. (ii) Experiments and studies of different types of terrestrial rocks weathered to various degrees have shown the existence of a small Mg isotopic fractionation between fluid and mineral (during either the dissolution of primary minerals or the formation of secondary minerals) of  $\Delta^{26}\text{Mg}_{\text{fluid-mineral}} < \approx -1\text{‰}$  (e. g. Ryu et al., 2016). Even though 10% in mass of Mg in the mesostases has been removed during secondary aqueous alteration, this would result in an upwards shift on the  $\delta^{25}\text{Mg}$  value by only  $\approx 0.10\text{‰}$ .

Very few  $\delta^{25}\text{Mg}$  variations can be expected between the various phases in chondrules if Mg isotopic equilibrium was established between them at the time of quenching during chondrule formation. In fact, studies on terrestrial mafic rocks have shown that stable Mg isotopic fractionation between silicate minerals like olivines and melts is almost negligible at temperatures above 1400 K ( $\leq 0.03\text{‰}$  on  $\delta^{25}\text{Mg}$ ; Teng et al., 2007). Thus, the intra-chondrule  $\delta^{25}\text{Mg}$  variations suggest the presence of relict isotopic heterogeneities from precursors and also some thermal processes that could affect specifically the Mg isotopic composition of the melted part of chondrules.

### 5.3. Effects of olivine dissolution and melt vaporization on Mg budgets of chondrule melts

Vaporization of Mg can be a possible source of Mg isotopic fractionation in chondrule melts, depending on the peak temperatures that chondrules reached during the heating events. In vacuum, a melt spherule can lose by evaporation  $\approx 0.2\%$  of its Mg per minute at 2000 K and  $\approx 3\%$  at 2200 K (Hashimoto et al., 1983; Floss et al., 1996; Davis et al., 1990; Table S8). On the other hand, the peak temperatures inferred by experimental analogs of chondrules range from  $< 1800$  K to 2200 K (Connolly and Love, 1998; Hewins and Radomsky, 1990; Connolly and Jones, 2016). In the cases of high peak temperatures of 1800-2200 K under vacuum (or a canonic partial pressure of Mg), chondrule melts would inevitably be subjected to Mg loss by evaporation.

It is also noticeable that some chondrules have only been partially molten, as evidenced by the presence in type I chondrules of  $^{16}\text{O}$ -rich olivines that are considered to be "relict" survivors from the chondrule precursors (Weinbruch et al., 1993; Jones et al., 2004; Pack et al., 2004; Chaussidon et al., 2008; Rudraswami et al., 2011; Tenner et al., 2013; Marrocchi et al., 2019a), and by the chemical disequilibrium between olivines/orthopyroxenes and mesostases (e.g., Libourel et al., 2006; Libourel and Chaussidon, 2011). This partially molten state for some chondrules can be corroborated by the existence of two internal  $^{26}\text{Al}$ - $^{26}\text{Mg}$  isochrons in the Leoville chondrule Leo-4337-t2-psB-c7 showing that all the phases in this chondrule were not re-equilibrated for Mg isotopes at the time of last melting event (Fig. 7I).

Therefore, partial melting of a Mg-rich precursor phase such as olivine must also be taken into account in the Mg budget of chondrule melts, together with potential Mg vaporization.

In a scenario combining melt evaporation and relict olivine dissolution, the Mg isotopic compositions of the chondrule melt are expected to be controlled by the thermal history of the chondrule. In detail, heating events would likely result in a competition between (i) Mg loss from chondrule melts by evaporation and (ii) Mg gain into chondrule melts by olivine dissolution (see the model in **Appendix**). The model results show that vaporization of Mg should lead to higher  $\delta^{25}\text{Mg}$  values in both the melt and the bulk chondrule. For a set  $T$ - $t$  paths, the scale of the changes in  $\delta^{25}\text{Mg}$  value is controlled by  $\alpha_{\text{gas-melt}}^{25/24}$ , which is 0.984-0.987 for evaporation in vacuum (Davis et al., 1990; Mendybaev et al., 2013) but can be close to unity at high Mg partial pressures in the ambient gases (e.g., Galy et al., 2000; Yu et al., 2003). For a chosen  $\alpha_{\text{gas-melt}}^{25/24}$  value (e.g., 0.999 in Fig. 9A), peak temperatures and cooling rates can affect the Mg fluxes by evaporation and olivine dissolution, thus impacting the  $\delta^{25}\text{Mg}$  values in chondrules. The higher peak temperatures or lower cooling rates result in more vaporization of Mg, and produce larger  $\delta^{25}\text{Mg}$  differences between chondrule melt and olivines (Fig. 9A).

It is important to note that magnesium evaporation associated with olivine dissolution can also impact the bulk  $\delta^{26}\text{Mg}^*$  values of chondrules. Before the extinction of  $^{26}\text{Al}$ , various degrees of radiogenic  $^{26}\text{Mg}$  enrichments can develop within the different phases of chondrule precursors before the last melting event took place. Under a partial melting scenario that has Mg-rich olivines as the relict components, preferential melting of the high- $^{27}\text{Al}/^{24}\text{Mg}$  phases within the chondrule precursors during heating events would produce melts carrying Mg

enriched in radiogenic  $^{26}\text{Mg}$  (in other words, the positive and high  $\delta^{26}\text{Mg}^*$  values), and Mg vaporization from such melts would deplete the radiogenic  $^{26}\text{Mg}$  from bulk chondrules, along with the increase in  $^{27}\text{Al}/^{24}\text{Mg}$  ratio. The replenishments of Mg from dissolution of olivines together with Mg losses by evaporation would force the  $\delta^{26}\text{Mg}^*$  values in the melt and the bulk of chondrule migrating towards the  $\delta^{26}\text{Mg}^*$  values of the olivines of precursors (Fig. 9B), which are supposed to be depleted in radiogenic  $^{26}\text{Mg}$  for their very low  $^{27}\text{Al}/^{24}\text{Mg}$  ratios. This evolution of  $\delta^{26}\text{Mg}^*$  in chondrule is sensitive to the peak temperatures and the cooling rates of the heating events. For instance, starting from a peak temperature of 2123 K can lead to decreases in bulk  $\delta^{26}\text{Mg}^*$  values of chondrules by 0.015‰ at a cooling rate of 500 K/h and by 0.008‰ at 1500K/h (Fig. 9B). The decreases in bulk  $\delta^{26}\text{Mg}^*$  values of chondrules would be significantly smaller when starting from a lower peak temperature of 2023 K, i.e., 0.005‰ at 500 K/h and by 0.002‰ at 1500K/h (Fig. 9B). Once the initial Mg in chondrule melt has been almost replaced by Mg from olivines, there would be  $(\delta^{26}\text{Mg}^*)_{\text{bulk}} \approx (\delta^{26}\text{Mg}^*)_{\text{melt}} \approx (\delta^{26}\text{Mg}^*)_{\text{olivine}_0}$  (Fig. 9B). If  $^{26}\text{Al}$  is not extinct yet at the time of chondrule quenching after the last heating event, the chondrule bulk  $\delta^{26}\text{Mg}^*$  value would increase till  $^{26}\text{Al}$  extinction (Fig. 9C), and show at present-day an internal  $^{26}\text{Al}$ - $^{26}\text{Mg}$  isochron, which dates the last melting event for chondrules.

#### 5.4. Implications for the formation of chondrules

The presence in chondrule melts of  $\delta^{25}\text{Mg}$  values 0.68-0.94‰ higher than in olivines for three of the studied chondrules implies, most likely, that these chondrules have experienced



some degrees of Mg evaporation, meaning that the peak temperatures of these chondrules have surpassed 1800 K over the last melting events. The lack of resolvable  $\delta^{25}\text{Mg}$  difference between olivines and mesostases within other chondrules (B-Ch1, Leo-4337-t2-ps2B-c2 and Leo-4337-t2-ps2B-c7) can be ascribed either to a completely molten state of the chondrule precursors or to a low peak temperature ( $< 1800$  K) during a possible re-heating event. The uncertainty of the effects from Mg partial pressure on the Mg evaporation rate and  $\alpha_{\text{gas-melt}}^{25/24}$  prevents us from defining the exact Mg fluxes by evaporation and those by olivine dissolution from the  $\delta^{25}\text{Mg}$  records. However, more information can be gained by knowing the  $\delta^{26}\text{Mg}^*$  data of bulk chondrules at a precision of 0.001-0.003‰, which is approachable thanks to improvements in solution MC-ICP-MS method (Larsen et al., 2011; Schiller et al., 2015; Olsen et al., 2016; van Kooten et al., 2016; Luu et al., 2019; Gregory et al., 2020).

There have been high-precision  $\delta^{26}\text{Mg}^*$  data in literature showing that chondrules with super-solar  $^{27}\text{Al}/^{24}\text{Mg}$  ratios ( $> 0.101$ ) can exhibit negative  $\delta^{26}\text{Mg}^*$  values down to  $-0.018 \pm 0.002$ ‰ (Olsen et al., 2016; van Kooten et al., 2016), which the authors have attributed to a reduced initial  $^{26}\text{Al}/^{27}\text{Al}$  ratios ( $1.5\text{-}2.2 \times 10^{-5}$ ) in the chondrule forming regions relative to the canonical  $^{26}\text{Al}/^{27}\text{Al}$  ratios of  $\approx 5 \times 10^{-5}$ . The distribution of initial  $^{26}\text{Al}$  abundance in the Solar System is so far a highly controversial topic with the co-existing arguments for either heterogeneity at  $\pm 80\%$  scale (e.g., Schiller et al., 2015; Olsen et al., 2016; Van Kooten et al., 2016; Bollard et al., 2017, 2019) or homogeneity with variations smaller than  $\pm 20\%$  (e.g., Jacobsen et al., 2008; Villeneuve et al., 2009; Budde et al., 2018; Luu et al., 2019; Gregory et al., 2020). We cannot solve this debate here, but we stress that a combination of Mg evaporation

and olivine dissolution during chondrule melting can lead to a preferential loss of Mg that is rich in radiogenic  $^{26}\text{Mg}$ . This mechanism is capable of producing negative bulk  $\delta^{26}\text{Mg}^*$  values in some chondrules with super-solar  $^{27}\text{Al}/^{24}\text{Mg}$  ratios (Fig. 9C). All these observations highlight the necessity of scrutinizing the phase relation inside chondrules from a metal stable isotope perspective (e.g., Mg, Si and Fe), which can help trace the thermal histories of chondrules during their formation.

It is noteworthy that if  $^{26}\text{Al}$  was homogeneously distributed in the solar nebula, forming chondrules with negative bulk  $\delta^{26}\text{Mg}^*$  values of  $-0.018\text{‰}$  from the precursors with initial  $\delta^{26}\text{Mg}^*$  value of  $-0.020\text{‰}$  would imply a strong vaporization of Mg, thus requiring the peak temperatures at chondrule melting to be significantly higher than 1800 K (up to 2123 K) and the cooling rates not to be too high ( $\leq 500$  K/h) (Fig. 9B, C). Applying the Mg fluxes of evaporation inferred from the  $\delta^{26}\text{Mg}^*$  records and the  $\delta^{25}\text{Mg}$  difference of  $+0.68$  to  $+0.94\text{‰}$  between chondrule melts and olivines, the  $\alpha_{\text{gas-melt}}^{25/24}$  value can be anchored to  $\approx 0.999$ . This value is much closer to unity compared to the values of 0.984-0.987 expected for evaporation in vacuum (Davis et al., 1990; Mendybaev et al., 2013), and rather points to a high Mg partial pressure in the ambient gases during chondrule formation (Galy et al., 2000; Yu et al., 2003). Such thermal and gas conditions are the most consistent with the conditions required for the shock wave model (Desch et al., 2012; Fedkin et al., 2012). In addition, the presence of Mg evaporation supports an "open" system for chondrules during their formation. This calls for revisiting the records of moderately volatile elements in chondrules. Earlier observations for the limited K isotopic variations (Humayun and Clayton, 1995; Alexander et al., 2000) and

absence of Na depletion (Alexander et al., 2008) suggest a "closed" system for chondrules during their last melting events. However, latest studies unravel that (i) chondrules have been depleted in Zn by two orders of magnitude and as well isotopically fractionated in Zn compared to the matrix (Pringle et al., 2017; van Kooten and Moynier, 2019), (ii) chondrules have higher Mn/Na ratios (up to 2) than bulk chondrites (around 0.3), likely pointing to depletion in Na (Mahan et al., 2018), and (iii) chondrules are significantly depleted in volatile elements relative to bulk chondrites (van Kooten et al., 2019).

## 5. Conclusions

(1) For *in situ* Mg isotopic measurements by LA-MC-ICP-MS,  $^{48}\text{Ca}^{2+}$  is the major doubly charged species interfering with the ions of Mg isotopes, and the productions of  $^{48}\text{Ti}^{2+}$  and  $^{52}\text{Cr}^{2+}$  are negligible. Monitoring together the intensities of  $^{44}\text{Ca}^{2+}$  and  $^{24}\text{Mg}^+$  under a sub cup configuration permits a sufficient correction of the  $^{48}\text{Ca}^{2+}$  interferences on  $^{24}\text{Mg}^+$ . The matrix-induced Mg isotopic fractionations are 1.0-1.5‰/amu for standards including olivines and komatiitic/basaltic/andesitic glasses, which are significantly smaller than those by SIMS (8‰/amu; Chaussidon et al., 2017). After the correction of  $^{48}\text{Ca}^{2+}$  interferences and matrix effects, the LA-MC-ICP-MS technique in this study is able to provide accurate Mg isotopic measurements with 2SD uncertainties of  $\pm 0.04$ - $0.06$ ‰ for olivines and of  $\pm 0.10$ - $0.60$ ‰ for mesostasis and melilite phases on the  $\delta^{26}\text{Mg}^*$  values, and of  $\pm 0.25$ - $0.30$ ‰ for olivines and of  $\pm 0.30$ - $0.55$ ‰ for mesostasis phases on the  $\delta^{25}\text{Mg}$  values.

(2) The internal  $^{26}\text{Al}$ - $^{26}\text{Mg}$  isochrons provide initial  $^{26}\text{Al}/^{27}\text{Al}$  ratios of  $5.46 (\pm 0.38) \times 10^{-5}$  to

$6.14 (\pm 0.92) \times 10^{-5}$  for the studied refractory inclusions and  $0.16 (\pm 0.08) \times 10^{-5}$  to  $1.87 (\pm 0.92) \times 10^{-5}$  for the chondrules, which are identical with uncertainty to literature values. The presence of Mg-rich olivines with low  $\delta^{25}\text{Mg}$  values in some type I chondrules implies that chondrule precursors may have formed via condensation of rapid-cooling gases, as similarly recorded by AOAs. Moreover, the higher  $\delta^{25}\text{Mg}$  values in mesostases than in olivines for three of the studied chondrules likely support Mg evaporation during the heating events.

(3) In a partial melting scenario for chondrule formation, peak temperature and cooling rate can impact on the Mg isotopic inventories of chondrules, via influencing the Mg fluxes by vaporization and by olivine dissolution. To produce the existing Mg isotopic observations under an assumption of homogeneous  $^{26}\text{Al}/^{27}\text{Al}$  as a function of time in the solar system, chondrules must have been heated up to high peak temperatures (up to 2123 K) and stayed above 1800 K for several tens of minutes during cooling to vaporize Mg, likely pointing to a heat source from shock wave for chondrule formation.

## Acknowledgements

We thank Pascale Louvat, Claire Rollion-Bard and Jessica Dallas for helping with the MC-ICP-MS and laser ablation system at IPGP. David Madre is appreciated for his help with the sample preparation for SIMS measurements at CRPG (Nancy). The Associate Editor Dimitri A. Papanastassiou and three anonymous reviewers are thanked for their constructive comments, which have improved significantly the manuscript. This work was supported by

ANR grant CRADLE (ANR-15-CE31-0004-01), and by the UnivEarthS Labex program (ANR-10-LABX-0023 and ANR-11-IDEX-0005-2).

## Appendix

### Formalism of non-mass dependent Mg isotopic effects from $^{48}\text{Ca}^{2+}$ , $^{48}\text{Ti}^{2+}$ and $^{52}\text{Cr}^{2+}$

After transformation, equations 3 can represent a multiplication factor on the true Mg isotope ion ratio:

$$\frac{\left( ^{25}\text{Mg} / ^{24}\text{Mg} \right)_{\text{meas}}}{\left( ^{25}\text{Mg}^+ / ^{24}\text{Mg}^+ \right)} = \frac{1}{1 + \left( ^{48}\text{Ca}^{2+} + ^{48}\text{Ti}^{2+} \right) / ^{24}\text{Mg}^+} \quad (\text{A1})$$

Similarly, equation 4 can be written as:

$$\frac{\left( ^{26}\text{Mg} / ^{24}\text{Mg} \right)_{\text{meas}}}{\left( ^{26}\text{Mg}^+ / ^{24}\text{Mg}^+ \right)} = \frac{1}{1 + \left( ^{48}\text{Ca}^{2+} + ^{48}\text{Ti}^{2+} \right) / ^{24}\text{Mg}^+} + \frac{^{52}\text{Cr}^{2+}}{^{24}\text{Mg}^+ + ^{48}\text{Ca}^{2+} + ^{48}\text{Ti}^{2+}} \times \frac{^{24}\text{Mg}^+}{^{26}\text{Mg}^+} \quad (\text{A2})$$

For all the samples in this study, the intensity of  $^{48}\text{Ca}^{2+}$  and  $^{48}\text{Ti}^{2+}$  is at maximum 0.3% of that of  $^{24}\text{Mg}^+$ . Thus:

$$\frac{1}{1 + \left( ^{48}\text{Ca}^{2+} + ^{48}\text{Ti}^{2+} \right) / ^{24}\text{Mg}^+} \approx 1 - \frac{^{48}\text{Ca}^{2+} + ^{48}\text{Ti}^{2+}}{^{24}\text{Mg}^+} \quad (\text{A3})$$

$$\frac{^{52}\text{Cr}^{2+}}{^{24}\text{Mg}^+ + ^{48}\text{Ca}^{2+} + ^{48}\text{Ti}^{2+}} \approx \frac{^{52}\text{Cr}^{2+}}{^{24}\text{Mg}^+} \quad (\text{A4})$$

As such, equations A1 and A2 can be approximated onto:

$$\frac{\left( ^{25}\text{Mg} / ^{24}\text{Mg} \right)_{\text{meas}}}{\left( ^{25}\text{Mg}^+ / ^{24}\text{Mg}^+ \right)} \approx 1 - \frac{^{48}\text{Ca}^{2+} + ^{48}\text{Ti}^{2+}}{^{24}\text{Mg}^+} \quad (\text{A5})$$

$$\frac{\left( ^{26}\text{Mg} / ^{24}\text{Mg} \right)_{\text{meas}}}{\left( ^{26}\text{Mg}^+ / ^{24}\text{Mg}^+ \right)} \approx 1 - \frac{^{48}\text{Ca}^{2+} + ^{48}\text{Ti}^{2+}}{^{24}\text{Mg}^+} + \frac{^{52}\text{Cr}^{2+}}{^{26}\text{Mg}^+} \quad (\text{A6})$$

Based on equation 2, the non-mass dependent Mg isotopic effects from  $^{48}\text{Ca}^{2+}$ ,  $^{48}\text{Ti}^{2+}$  and  $^{52}\text{Cr}^{2+}$

(noted as  $\Delta^{26}\text{Mg}_{\text{Ca+Ti+Cr}}$ ) should be:

$$\Delta^{26}\text{Mg}_{\text{Ca+Ti+Cr}} \approx \left\{ \frac{\left( \frac{^{26}\text{Mg}}{^{24}\text{Mg}} \right)_{\text{meas}}}{\left( \frac{^{26}\text{Mg}^+}{^{24}\text{Mg}^+} \right)} - 1 - \left[ \frac{\left( \frac{^{25}\text{Mg}}{^{24}\text{Mg}} \right)_{\text{meas}}}{\left( \frac{^{25}\text{Mg}^+}{^{24}\text{Mg}^+} \right)} - 1 \right] \times \frac{1}{\beta_{\text{mtr}}} \right\} \times 10^3 \quad (\text{A7})$$

Substituting equations A5 and A6 into equation A7 provides:

$$\Delta^{26}\text{Mg}_{\text{Ca+Ti+Cr}} \approx \left[ \frac{^{48}\text{Ca}^{2+} + ^{48}\text{Ti}^{2+}}{^{24}\text{Mg}^+} \times \left( \frac{1}{\beta_{\text{mtr}}} - 1 \right) + \frac{^{52}\text{Cr}^{2+}}{^{26}\text{Mg}^+} \right] \times 10^3 \quad (\text{A8})$$

Since  $\beta_{\text{mtr}} = 0.517$  has been chosen in this study, we have:

$$\frac{1}{\beta_{\text{mtr}}} - 1 \approx 0.934 \quad (\text{A9})$$

The  $^{48}\text{Ca}^{2+}/^{24}\text{Mg}^+$  ratios of samples can be written:

$$\frac{^{48}\text{Ca}^{2+}}{^{24}\text{Mg}^+} = \frac{^{44}\text{Ca}^{2+}}{^{24}\text{Mg}^+} \times \frac{^{48}\text{Ca}^{2+}}{^{44}\text{Ca}^{2+}} \quad (\text{A10})$$

Substituting equations A9 and A10 into equation A8 provides:

$$\Delta^{26}\text{Mg}_{\text{Ca+Ti+Cr}} \approx \left( 0.934 \times \frac{^{44}\text{Ca}^{2+}}{^{24}\text{Mg}^+} \times \frac{^{48}\text{Ca}^{2+}}{^{44}\text{Ca}^{2+}} + 0.934 \times \frac{^{48}\text{Ti}^{2+}}{^{24}\text{Mg}^+} + \frac{^{52}\text{Cr}^{2+}}{^{26}\text{Mg}^+} \right) \times 10^3 \quad (\text{A11})$$

### Modeling Al-Mg inventory of chondrules in a scenario combining olivine dissolution and Mg evaporation

The vaporization of Mg in vacuum (Hashimoto et al., 1983; Floss et al., 1996; Davis et al., 1990) can be fitted by an empirical fourth-power function of temperature (Table S8):

$$r_{\text{evap}} \approx \left[ 0.000959(\pm 0.000044) \times T - 1.702(\pm 0.093) \right]^4 \quad (\text{A12})$$

with  $r_{\text{evap}}$  the evaporation rate of Mg that is described as the fraction of total Mg per minute

and  $T$  the temperature in K. The Mg evaporation rate starts to be significant above 1800 K,

and rises rapidly with temperature. In a reservoir with high dust-enrichments, vaporization can increase partial pressures of Mg in the gases, and therefore reduce the vaporization rate of Mg or lead to some re-condensation. For instance, based on cathodoluminescence mapping of Mg-rich olivines in a set of type I chondrules, Libourel and Portail (2018) inferred that the olivines had likely grown in a melt experiencing Mg and Si exchanges with the surrounding gas. However, experiments investigating Mg evaporation from silicate melts at non-vacuum gaseous environments are currently not available. Hence, we assume that equation A12 also applies to the case of chondrule melting, but we mitigate the uncertainty from this assumption by considering various gas-melt Mg isotopic fractionation factors during evaporation.

As described in Soulié et al. (2017), the olivine dissolution rate ( $\tau_{\text{dissol}}$  in  $\mu\text{m}/\text{min}$  after a spherical approximation) in a melt follows:

$$\tau_{\text{dissol}} \approx A_0 \times e^{-E_a/RT} \quad (\text{A13})$$

where  $A_0$  and  $E_a$  are Arrhenius parameters, representing pre-exponential factor and activation energy, respectively. Note that  $A_0$  and  $E_a$  would vary with different melt compositions (such as anorthite, spinel and tridymite; Soulié et al., 2017).

For a given thermal history,

$$T = f(t) \quad (\text{A14})$$

where  $t$  represents the time in minute since the beginning of the selected time window, the rates of Mg evaporation and olivine dissolution can be calculated from equations A12 and A13.

To compare the effects from Mg evaporation and olivine dissolution, the Mg fluxes from the two processes can be both described as the fraction of the total Mg in the initial system,

e.g., the Mg budget of the system will be smaller than "1" after some Mg evaporation. To start the modeling, we assume for the chondrule precursors:  $\delta^{25}\text{Mg}_{\text{non-olivine or olivine}_0} = 0\%$ ,  $(^{27}\text{Al}/^{24}\text{Mg})_{\text{bulk}_0} = 0.101$ ,  $(^{27}\text{Al}/^{24}\text{Mg})_{\text{olivine}_0} = 0.001$ ,  $(^{27}\text{Al}/^{24}\text{Mg})_{\text{non-olivine or melt}_0} = 2.011$ ,  $F_{\text{Mg-non-olivine}_0} = 0.05$  and  $F_{\text{Mg-olivine}_0} = 0.95$ , where  $F$  represents the fraction of total Mg in the precursors (olivine and non-olivine). The choice of  $F_{\text{Mg-olivine}_0} = 0.95$  for the precursors is based on the fact that the Mg budget of a type I PO chondrule is dominated by olivine. The simplest scenario is to assume that the non-olivine phases will be preferentially melted upon heating, i.e.  $F_{\text{Mg-melt}_0} \approx F_{\text{Mg-non-olivine}_0}$ . The Mg flux per minute to the melt due to olivine dissolution ( $\Delta F_{\text{dissol}}$ ) over an incremental time,  $\Delta t$ , interval between  $t_i$  and  $t_j$  ( $t_j = t_i + \Delta t$ ) can be quantified as:

$$\Delta F_{\text{dissol}-t_i-t_j} = \left[ F_{\text{Mg-olivine}-t_i} - \left( \frac{\sqrt[3]{F_{\text{Mg-olivine}-t_i}} \times R - \tau_{\text{dissol}-t_i} \times \Delta t}{\sqrt[3]{F_{\text{Mg-olivine}-t_i}} \times R} \right)^3 \right] \quad (\text{A15})$$

with  $\tau_{\text{dissol}-t_i}$  the olivine dissolution rate at  $t_i$  in  $\mu\text{m}/\text{min}$  derived by combining equations A13 and A14,  $R$  the initial average radius of olivines in  $\mu\text{m}$  considering a spherical approximation,  $F_{\text{Mg-olivine}-t_i}$  the Mg fraction in olivine at  $t_i$ , and  $\Delta F_{\text{dissol}-t_i-t_j}$  the Mg flux from olivine dissolution from  $t_i$  to  $t_j$ . By comparison, the Mg flux from evaporation ( $\Delta F_{\text{evap}-t_i-t_j}$ ) between  $t_i$  and  $t_j$  would be:

$$\Delta F_{\text{evap}-t_i-t_j} = r_{\text{evap}-t_i} \times \Delta t \quad (\text{A16})$$

with  $r_{\text{evap}-t_i}$  the Mg evaporation rate at  $t_i$  in unit of fraction of total Mg per minute.

It is however noteworthy that the temperature-dependent function for olivine dissolution in equation A13 is valid only when the melt composition did not change much with olivine



dissolution. In other words, the melt reservoir has to be large and merely affected by input from the dissolving olivine. Nonetheless, most type I chondrules have high olivine/melt ratios, in which olivine dissolution would have a strong impact on the composition of chondrule melts, and therefore also on the olivine dissolution rate. As shown by the experiments using starting materials with chondrule-like olivine/melt ratios in Villeneuve et al. (2015), olivine dissolution rate can be reduced by 2-3 orders of magnitude when the SiO<sub>2</sub> and MgO contents start to be high in the melts due to olivine dissolution. Substituting  $R = 1000 \text{ } \mu\text{m}$  and the olivine dissolution parameters of an 'anorthite'-like melt composition from Soulié et al. (2017) into equation A15 shows that the Mg fluxes of olivine dissolution in a melt that is strongly under-saturated in olivine can surpass the Mg fluxes of evaporation by 2 orders of magnitude. As such, a more realistic situation for the Mg fluxes in chondrule melt should be: (i) olivine dissolution occurs but ceases quickly through saturating the melt in olivine and (ii) olivine dissolution proceeds with olivine under-saturation in the melt created by evaporation. As such, instead of equations A13, the Mg fluxes of olivine dissolution between  $t_i$  and  $t_j$  can be approximated to be the same as those of vaporization:

$$\Delta F_{\text{dissol-}t_i-t_j} = \Delta F_{\text{evap-}t_i-t_j} \quad (\text{A17})$$

The Mg fractions and <sup>27</sup>Al/<sup>24</sup>Mg ratio in olivine, melt and bulk system at  $t_j$  should follow mass conservation (assuming that Al is not evaporated from the chondrule melt):

$$F_{\text{Mg-olivine-}t_j} = F_{\text{Mg-olivine-}t_i} - \Delta F_{\text{dissol-}t_i-t_j} \quad (\text{A18})$$

$$F_{\text{Mg-melt-}t_j} = F_{\text{Mg-melt-}t_i} - \Delta F_{\text{evap-}t_i-t_j} + \Delta F_{\text{dissol-}t_i-t_j} \quad (\text{A19})$$

$$\left(\frac{{}^{27}\text{Al}}{{}^{24}\text{Mg}}\right)_{\text{melt}-t_j} = \left(\frac{{}^{27}\text{Al}}{{}^{24}\text{Mg}}\right)_{\text{melt}-t_i} \times \left(\frac{F_{\text{Mg-melt}-t_i}}{F_{\text{Mg-melt}-t_j}}\right) \quad (\text{A20})$$

$$\left(\frac{{}^{27}\text{Al}}{{}^{24}\text{Mg}}\right)_{\text{bulk}-t_j} = \left(\frac{{}^{27}\text{Al}}{{}^{24}\text{Mg}}\right)_{\text{bulk}_0} \times \frac{1}{F_{\text{Mg-olivine}-t_j} + F_{\text{Mg-melt}-t_j}} \quad (\text{A21})$$

Once Mg evaporation occurs, the  ${}^{27}\text{Al}/{}^{24}\text{Mg}$  ratio in bulk chondrule would increase, whereas the  ${}^{27}\text{Al}/{}^{24}\text{Mg}$  ratios of chondrule melt should be stable due to the cancel-out of the Mg fluxes from evaporation and olivine dissolution. For the  $\delta^{25}\text{Mg}$  values, it can be approximated into a two-step process in a small time-interval. The remaining Mg in chondrule melt at  $t_j$  after evaporation would tend to be more enriched in the heavy isotopes following:

$$\delta^{25}\text{Mg}_{\text{melt-evap}-t_i} = \delta^{25}\text{Mg}_{\text{melt}-t_i} - 1000 \times \left(\alpha_{\text{gas-melt}}^{25/24} - 1\right) \times \frac{\Delta F_{\text{evap}-t_i-t_j}}{F_{\text{Mg-melt}-t_i}} \quad (\text{A22})$$

The Mg gain from olivine dissolution brings the  $\delta^{25}\text{Mg}$  values of chondrule melt at  $t_j$  to:

$$\delta^{25}\text{Mg}_{\text{melt}-t_j} = \delta^{25}\text{Mg}_{\text{melt-evap}-t_i} \times \frac{F_{\text{Mg-melt}-t_i} - \Delta F_{\text{evap}-t_i-t_j}}{F_{\text{Mg-melt}-t_j}} + \delta^{25}\text{Mg}_{\text{olivine}_0} \times \frac{\Delta F_{\text{dissol}-t_i-t_j}}{F_{\text{Mg-melt}-t_j}} \quad (\text{A23})$$

The  $\delta^{25}\text{Mg}$  values of bulk chondrule at  $t_j$  would then be:

$$\delta^{25}\text{Mg}_{\text{bulk}-t_j} = \frac{\delta^{25}\text{Mg}_{\text{olivine}_0} \times F_{\text{Mg-olivine}-t_j} + \delta^{25}\text{Mg}_{\text{melt}-t_j} \times F_{\text{Mg-melt}-t_j}}{F_{\text{Mg-olivine}-t_j} + F_{\text{Mg-melt}-t_j}} \quad (\text{A24})$$

We model below, for the sake of the exercise, a case where the precursors (olivine + matrix phases) were condensed from a canonic gas at 0.717 Myr after CAIs (i.e., one half-life for  ${}^{26}\text{Al}$ ) and the chondrule heating took place 2 Myr after CAIs, in agreement with general  ${}^{26}\text{Al}$ - ${}^{26}\text{Mg}$  chronologies of chondrules reconstructed assuming a homogeneous  ${}^{26}\text{Al}/{}^{27}\text{Al}$  as a function of time (i.e., last melting events at 1-3 Myr after CAIs and precursors which can be nearly as old as CAIs, e.g., Kita et al., 2000; Villeneuve et al., 2009; Luu et al., 2015; Gregory et al., 2020).

We consider thereafter for the precursors:  $({}^{27}\text{Al}/{}^{24}\text{Mg})_{\text{bulk}_0} = 0.101$ ,  $({}^{27}\text{Al}/{}^{24}\text{Mg})_{\text{olivine}_0} = 0.001$ ,

$(^{27}\text{Al}/^{24}\text{Mg})_{\text{non-olivine or melt}_0} = 2.011$ ,  $F_{\text{Mg-non-olivine}_0} = 0.05$  and  $F_{\text{Mg-olivine}_0} = 0.95$ . Assuming initial  $^{26}\text{Al}/^{27}\text{Al}$  ratio and  $\delta^{26}\text{Mg}^*$  value of  $5.23 \times 10^{-5}$  and  $-0.040\text{‰}$ , respectively, for the solar nebula (Jacobsen et al., 2008; Villeneuve et al., 2009, 2011; Luu et al., 2015; Chen et al., 2018; Gregory et al., 2020), the chondrule precursor would have  $(\delta^{26}\text{Mg}^*)_{\text{bulk}} = (\delta^{26}\text{Mg}^*)_{\text{olivine}} = (\delta^{26}\text{Mg}^*)_{\text{non-olivine}} = -0.020\text{‰}$  at 0.717 Myrs after CAIs, evolving to  $(\delta^{26}\text{Mg}^*)_{\text{bulk}} \approx -0.003\text{‰}$ ,  $(\delta^{26}\text{Mg}^*)_{\text{olivine}} \approx -0.020\text{‰}$  and  $(\delta^{26}\text{Mg}^*)_{\text{non-olivine or melt}} \approx +0.326\text{‰}$  at the time of heating (2 Myr after CAIs). The  $\delta^{26}\text{Mg}^*$  values of the melt and the bulk of chondrule at  $t_j$  after melt evaporation and olivine dissolution are given by:

$$(\delta^{26}\text{Mg}^*)_{\text{melt}-t_j} \approx \frac{(\delta^{26}\text{Mg}^*)_{\text{melt}-t_i} \times (F_{\text{Mg-melt}-t_i} - \Delta F_{\text{evap}-t_i-t_j}) + (\delta^{26}\text{Mg}^*)_{\text{olivine}_0} \times \Delta F_{\text{dissol}-t_i-t_j}}{F_{\text{Mg-melt}-t_j}} \quad (\text{A25})$$

$$(\delta^{26}\text{Mg}^*)_{\text{bulk}-t_j} \approx \frac{(\delta^{26}\text{Mg}^*)_{\text{olivine}_0} \times F_{\text{Mg-olivine}-t_j} + (\delta^{26}\text{Mg}^*)_{\text{melt}-t_j} \times F_{\text{Mg-melt}-t_j}}{F_{\text{Mg-olivine}-t_j} + F_{\text{Mg-melt}-t_j}} \quad (\text{A26})$$

For any other chondrule precursors and  $T$ - $t$  paths, the time-integrated  $^{27}\text{Al}/^{24}\text{Mg}$  ratios as well as the  $\delta^{25}\text{Mg}$  and  $\delta^{26}\text{Mg}^*$  values of chondrule melt or bulk chondrule can be obtained via iteration of equations A12, A14 and A16 to A26. Note that under the approximation of  $\Delta F_{\text{dissol}-t_i-t_j} = \Delta F_{\text{evap}-t_i-t_j}$ , the Mg evaporation histories of chondrules can be reconstructed from their Mg isotopic records.

## Figures and captions

**Fig. 1.** Plot of  $\Delta^{26}\text{Mg}_{\text{Ca+Ti+Cr}}/1000$  versus measured  $^{44}\text{Ca}^{2+}/^{24}\text{Mg}^+$  ratios for mineral and glass standards. The raw Mg isotopic ratios have included the isobaric interferences from doubly charged ions including  $^{48}\text{Ca}^{2+}$ ,  $^{48}\text{Ti}^{2+}$  and  $^{52}\text{Cr}^{2+}$ . The four types of symbols (i.e., circle, diamond,

square, triangle) represent the data from four sessions (Tables S3 to S6), with the circle for the Allende session with a linear regression of  $y = (0.097 \pm 0.005) x + (0.000017 \pm 0.000019)$ , the diamond for the Leoville session with  $y = (0.097 \pm 0.005) x + (0.000017 \pm 0.000019)$ , and the triangle and square for the other two sessions including only mineral and glass standards with  $y = (0.091 \pm 0.004) x + (0.000073 \pm 0.000058)$  and  $y = (0.100 \pm 0.001) x + (0.000042 \pm 0.000014)$ . The CMAS glasses have been marked with the lighter colors to be distinguished from the olivines and komatiitic/basaltic/andesitic glasses.

**Fig. 2.** (A) Plot of measured  $^{44}\text{Ca}^{2+}/^{24}\text{Mg}^+$  ratios versus true  $^{44}\text{Ca}/^{24}\text{Mg}$  ratios and (B) plot of measured  $^{27}\text{Al}^+/^{24}\text{Mg}^+$  ratios versus true  $^{27}\text{Al}/^{24}\text{Mg}$  ratios for mineral and glass standards. Symbols are the same as those in Fig. 1. The sessions using spot sizes of 40  $\mu\text{m}$  to 65  $\mu\text{m}$  (i.e., the circle, diamond and square) are providing a single well-defined linear regression for each session. For the session with a large spot size of 110  $\mu\text{m}$  (i.e., the triangle), the CMAS glasses (i.e., the light green triangle) form a calibration line different from that defined by olivines and komatiitic/basaltic/andesitic glasses (i.e., the green triangle). It is noteworthy that the  $^{27}\text{Al}/^{24}\text{Mg}$  and  $^{44}\text{Ca}/^{24}\text{Mg}$  ratios for individual ablation spots on chondrules can be derived using the correlations in (A) and (B), which together with the Mg ion intensities can help discriminate well the ablated phases.

**Fig. 3.** Plot of  $[\delta^{25}\text{Mg}_{\text{measured}} - \delta^{25}\text{Mg}_{\text{true}}]$  values caused by matrix effects versus MINBS values for mineral and glass standards in (A) Allende and Leoville sessions with San Carlos olivines as the bracketing standards and (B) the other two sessions on only standards with BHVO-2G or BIR-1G glass as the bracketing standard. Symbols are the same as those in Fig. 1. Relative

to the systematics from olivines, komatiitic/basaltic/andesitic glasses, diopside and crystalline MORB, the CMAS glasses deviate to the lower  $[\delta^{25}\text{Mg}_{\text{measured}} - \delta^{25}\text{Mg}_{\text{true}}]$  values at a low laser fluence of 3.37 or 4.23 J/cm<sup>2</sup>, but higher values at a high laser fluence of 11.47 J/cm<sup>2</sup>.

Fig. 4. Plot of true  $^{44}\text{Ca}/^{24}\text{Mg}$  ratios versus true  $^{27}\text{Al}/^{24}\text{Mg}$  ratios for the chondrule phases and refractory inclusions in Allende and Leoville, as well as the used mineral and glass standards. Note that the measured chondrule phases have the chemical compositions resembling to those of the used olivines and komatiitic/basaltic/andesitic glasses.

**Fig. 5.** (A) Plot of  $\delta^{25}\text{Mg}_{\text{bracketing standard}}$  versus  $\delta^{26}\text{Mg}_{\text{bracketing standard}}$  and (B) plot of measured  $\delta^{26}\text{Mg}^*$  versus true  $^{27}\text{Al}/^{24}\text{Mg}$  for mineral and glass standards. Symbols are the same as those in Fig. 1. After removing  $^{48}\text{Ca}^{2+}$  interferences, all the terrestrial standards are plotting along a mass-dependent fractionation line in (A), in other words along a 'zero' baseline in (B) despite the  $^{27}\text{Al}/^{24}\text{Mg}$  ratios. The results without correction of  $^{48}\text{Ca}^{2+}$  are shown by the same types of symbols but in dashed, which reveal that  $^{48}\text{Ca}^{2+}$  interferences can lead to erroneously positive  $\delta^{26}\text{Mg}^*$  values if not being properly corrected.

**Fig. 6.** Comparing the  $\delta^{25}\text{Mg}$  values by LA-MC-ICP-MS and those by solution MC-ICP-MS method from mineral and glass standards. Symbols are the same as those in Fig. 1. The  $\delta^{25}\text{Mg}$  values by LA-MC-ICP-MS here are after correction of  $^{48}\text{Ca}^{2+}$  and matrix effects. Note that applying the olivines and komatiitic/basaltic/andesitic glass standards to correct matrix effects has biasedly resulted in the higher  $\delta^{25}\text{Mg}$  values at a high laser fluence of 11.47 J/cm<sup>2</sup> whereas the lower  $\delta^{25}\text{Mg}$  values at a low laser fluence of 3.37 or 4.23 J/cm<sup>2</sup> for the CMAS glasses by LA-MC-ICP-MS.

**Fig. 7.** Internal  $^{26}\text{Al}$ - $^{26}\text{Mg}$  isochrons of the studied Allende and Leoville refractory inclusions (**A-C**) and chondrules (**D-I**), with the red square for the spots on olivines and orthopyroxenes, the blue square for those on Al-rich phases (e.g., glassy mesostases, clinopyroxene, melilite, spinel and plagioclase). The results by SIMS are represented by green square in (**D**) and (**E**). The regression data are calculated with the Model 1 in Isoplot 4.15 (Ludwig, 2008). Probably due to late disturbance, three spots have been excluded from the  $^{26}\text{Al}$ - $^{26}\text{Mg}$  isochron of the Allende melilite Mel-1 in (**A**). For chondrule Leo-4337-t2-ps2B-c7, there are possibly two internal  $^{26}\text{Al}$ - $^{26}\text{Mg}$  isochrons, and those spots plotting close to the bulk CAI  $^{26}\text{Al}$ - $^{26}\text{Mg}$  isochron (Jacobsen et al., 2008; Larsen et al., 2011) have been highlighted in orange symbols.

**Fig. 8.** Plot comparing  $\delta^{25}\text{Mg}$  variations in the studied chondrules and AOA. The literature data for bulk chondrules (Galy et al., 2000; Bizzarro et al., 2004; Bouvier et al., 2013; Luu et al., 2015; Olsen et al., 2016; van Kooten et al., 2016; Chen et al., 2018) and AOAs (Larsen et al., 2011) (Table S7) are shown for comparison.

**Fig. 9.** Modeling of the changes of (**A**) melt-olivine  $\delta^{25}\text{Mg}$  difference and (**B**) bulk  $\delta^{26}\text{Mg}^*$  value, and (**C**) the bulk  $\delta^{26}\text{Mg}^*$  versus bulk  $^{27}\text{Al}/^{24}\text{Mg}$  systematics in the case of chondrule precursors submitted to heating events at 2 Ma with a peak temperature of 2023 K or 2123 K and a cooling rate of 500 K/h or 1500 K/h in a scenario combining melt evaporation and olivine dissolution. The olivines of the precursors are supposed to have an age of 0.717 Ma and thus to have  $\delta^{26}\text{Mg}^* = -0.020\text{‰}$  (see detailed descriptions on chemical composition of precursors in **Appendix**). A  $\alpha^{25/24}$  (gas-melt) value of 0.999 has been used in (**A**) to quantify mass-dependent Mg isotopic fractionations in chondrules. The light orange field in (**C**) illustrates the

theoretical field for bulk chondrules under the assumptions of (i) a closed system for chondrules during the last heating events and (ii) a canonic  $^{26}\text{Al}$  distribution in the solar nebula (i.e.  $^{26}\text{Al}$  homogeneity with initial  $^{26}\text{Al}/^{27}\text{Al}$  ratio and  $\delta^{26}\text{Mg}^*$  value of  $5.23 \times 10^{-5}$  and  $-0.040\%$ , respectively). The model (red trajectory calculated at the time of heating) shows that Mg evaporation coupled to olivine dissolution is capable of making chondrules plotting out of the light orange field, which therefore cannot be considered to support unequivocally a  $^{26}\text{Al}$  heterogeneity in the solar nebula (C). The grey trajectory in (C) is the present-day equivalent to the red trajectory considering the addition of radiogenic  $^{26}\text{Mg}$  from further  $^{26}\text{Al}$  decay after the time of chondrule mesostasis quenching.

## References

- Alexander C.O'D., Grossman J.N., Wang J., Zanda B., Bourot-Denise M. and Hewins R.H. (2000) The lack of potassium-isotopic fractionation in Bishunpur chondrules. *Meteorit. Planet. Sci.* 35: 859–868.
- Alexander C.O'D. and Grossman J.N. (2005) Alkali elemental and potassium isotopic compositions of Semarkona chondrules. *Meteorit. Planet. Sci.* 40: 541–556.
- Alexander C.O'D., Grossman J.N., Ebel D.S. and Ciesla F.J. (2008) The formation conditions of chondrules and chondrites. *Science*, 320: 1617–1619.
- Asphaug E., Jutzi M. and Movshovitz N. (2011) Chondrule formation during planetesimal accretion. *Earth Planet. Sci. Lett.* 308: 369–379.

- Bizzarro M., Baker J.A. and Haack H. (2004) Mg isotope evidence for contemporaneous formation of chondrules and refractory inclusions. *Nature* 431: 275–278.
- Bouvier A., Wadhwa M., Simon S.B. and Grossman L. (2013) Magnesium isotopic fractionation in chondrules from the Murchison and Murray CM2 carbonaceous chondrites. *Meteorit. Planet. Sci.* 48: 339–353.
- Budde G., Kruijer T.S., Kleine T. (2018) Hf-W chronology of CR chondrites: Implications for the timescales of chondrule formation and the distribution of  $^{26}\text{Al}$  in the solar nebula. *Geochim. Cosmochim. Acta* 222: 284–304.
- Bollard J., Connelly J.N., Whitehouse M.J., Pringle E.A., Bonal L., Jørgensen J.K., Nordlund Å., Moynier F., Bizzarro M. (2017) Early formation of planetary building blocks inferred from Pb isotopic ages of chondrules. *Sci. Adv.* 3: e1700407.
- Bollard J., Kawasaki N., Sakamoto N., Olsen M., Itoh S., Larsen K., Wielandt D., Schiller M., Connelly J.N., Yurimoto H. and Bizzarro M. (2019) Combined U-corrected Pb-Pb dating and  $^{26}\text{Al}$ - $^{26}\text{Mg}$  systematics of individual chondrules—Evidence for a reduced initial abundance of  $^{26}\text{Al}$  amongst inner Solar System chondrules. *Geochim. Cosmochim. Acta* 260: 62–83.
- Catanzaro E. J., Murphy T. J., Garner E. L., Shields W. R. (1966) Absolute isotopic abundance ratios and atomic weight of magnesium. *J. Res. Natl. Bur. Stand. A Phys. Chem.* 70A: 453–458.
- Chaussidon M., Deng Z., Villeneuve J., Moureau J., Watson B., Richter F. and Moynier F. (2017) In situ analysis of non-traditional isotopes by SIMS and LA–MC–ICP–MS: Key



- aspects and the example of Mg isotopes in olivines and silicate glasses. *Rev. Mineral. Geochem.* 82: 127–163.
- Chaussidon M., Libourel G., Krot A.N. (2008) Oxygen isotopic constraints on the origin of magnesian chondrules and on the gaseous reservoirs in the early Solar System. *Geochim. Cosmochim. Acta* 72: 1924–1938.
- Chen H.W., Claydon J.L., Elliott T., Coath C.D., Lai Y.J. and Russell S.S. (2018) Chronology of formation of early solar system solids from bulk Mg isotope analyses of CV3 chondrules. *Geochim. Cosmochim. Acta* 227: 19–37.
- Clayton R.N., Hinton, R.W. and Davis, A.M. (1988) Isotopic variations in the rock-forming elements in meteorites. *Philos. Trans. Royal Soc. A* 325: 483–501.
- Clayton R.N. (1993) Oxygen isotopes in meteorites. *Annu. Rev. Earth Planet. Sci.* 21: 115–149.
- Clayton R.N. and Mayeda T.K. (1999) Oxygen isotope studies of carbonaceous chondrites. *Geochim. Cosmochim. Acta* 63: 2089–2104.
- Connolly H.C. and Jones R.H. (2016) Chondrules: The canonical and non-canonical view. *J. Geophys. Res. Planets.* 121: 1885–1899.
- Connolly H.C., Jones B.D. and Hewins R.H. (1998) The flash melting of chondrules: An experimental investigation into the melting history and physical nature of chondrule precursors. *Geochim. Cosmochim. Acta* 62: 2725–2735.
- Connolly H.C. and Love S.G. (1998) The formation of chondrules: Petrologic tests of the shock wave model. *Science* 280: 62–67.

- Davis A.M., Hashimoto A., Clayton R.N. and Mayeda T.K. (1990) Isotope mass fractionation during evaporation of  $\text{Mg}_2\text{SiO}_4$ . *Nature* 347: 655–658.
- Davis A.M., Richter F.M., Mendybaev R.A., Janney P.E., Wadhwa M. and McKeegan K.D. (2015) Isotopic mass fractionation laws for magnesium and their effects on  $^{26}\text{Al}$ – $^{26}\text{Mg}$  systematics in solar system materials. *Geochim. Cosmochim. Acta* 158: 245–261.
- Desch S.J., Morris M.A., Connolly H.C., and Boss A.P. (2012) The importance of experiments: Constraints on chondrule formation models. *Meteorit. Planet. Sci.* 47: 1139–1156.
- Ebel D.S., Alexander C.M.O'D. and Libourel G. (2018) Vapor-melt exchange-Constraints on chondrule formation conditions and processes. In *Chondrules*. Eds. S. Russell, A. Krot and H.C. Connolly Jr. Cambridge U. Press. pp. 151–174.
- Ebel D.S., Brunner C., Konrad K., Leftwich K., Erb I., Lu M., Rodriguez H., Crapster-Pregont E.J., Friedrich J.M. and Weisberg M.K. (2016) Abundance, major element composition and size of components and matrix in CV, CO and Acfer 094 chondrites. *Geochim. Cosmochim. Acta* 172: 322–356.
- Fedkin A.V., Grossman L., Ciesla F.J. and Simon S.B. (2012) Mineralogical and isotopic constraints on chondrule formation from shock wave thermal histories. *Geochim. Cosmochim. Acta* 87: 81–116.
- Floss C., El Goresy A., Zinner E., Kransel G., Rammensee W. and Palme H. (1996) Elemental and isotopic fractionations produced through evaporation of the Allende CV chondrite: Implications for the origin of HAL-type hibonite inclusions. *Geochim. Cosmochim. Acta* 60: 1975–1997.

- Friedrich J.M., Weisberg M.K., Ebel D.S., Biltz A.E., Corbett B.M., Iotzov I.V., Khan W.S. and Wolman M.D. (2015) Chondrule size and related physical properties: A compilation and evaluation of current data across all meteorite groups. *Chemie der Erde*, 75: 419–443.
- Fukuda K., Beard B.L., Dunlap D.R., Spicuzza M.J., Fournelle J.H., Wadhwa M., Kita N.T. (2020) Magnesium isotope analysis of olivine and pyroxene by SIMS: Evaluation of matrix effects. *Chem. Geol.* 540: 119482.
- Fukuda K., Brownlee D.E., Joswiak D.J., Tenner T.J., Kimura M., Kita N.T. (2021) Correlated isotopic and chemical evidence for condensation origins of olivine in comet 81P/Wild 2 and in AOAs from CV and CO chondrites. *Geochim. Cosmochim. Acta.* 293: 544–574.
- Galy A., Young E.D., Ash R.D. and O'Nions R.K. (2000) The formation of chondrules at high gas pressures in the solar nebula. *Science* 290: 1751–1753.
- Galy A., Yoffe O., Janney P.E., Williams R.W., Cloquet C., Alard O., Halicz L., Wadhwa M., Hutcheon I.D., Ramon E. and Carignan (2003) Magnesium isotope heterogeneity of the isotope standard SRM980 and new reference materials for magnesium-isotope-ratio measurements. *J. Anal. Atom. Spectrom.* 18: 1352–1356.
- Gregory T., Luu T.H., Coath C.D., Russell S.S. and Elliott T. (2020) Primordial formation of major silicates in a protoplanetary disc with homogeneous  $^{26}\text{Al}/^{27}\text{Al}$ . *Sci. Adv.* 6. DOI: 10.1126/sciadv.aay9626
- Hashimoto A. (1983) Evaporation metamorphism in the early solar nebula—Evaporation experiments on the melt  $\text{FeO-MgO-SiO}_2\text{-CaO-Al}_2\text{O}_3$  and chemical fractionations of primitive materials. *Geochem. J.* 17: 111–145.

- Hashimoto A. (1990) Evaporation kinetics of forsterite and implications for the early solar nebula. *Nature* 347: 53–55.
- Hewins R.H. and Fox G.E. (2004) Chondrule textures and precursor grain size: an experimental study. *Geochim. Cosmochim. Acta* 68: 917–926.
- Hewins R.H. and Radomsky P.M. (1990) Temperature conditions for chondrule formation. *Meteorit. Planet. Sci.* 25: 309–318.
- Humayun M. and Clayton R.N. (1995) Potassium isotope cosmochemistry: Genetic implications of volatile element depletion. *Geochim. Cosmochim. Acta* 59: 2131–2148.
- Jacobsen B., Yin Q.Z., Moynier F., Amelin Y., Krot A.N., Nagashima K., Hutcheon I.D. and Palme H. (2008)  $^{26}\text{Al}$ – $^{26}\text{Mg}$  and  $^{207}\text{Pb}$ – $^{206}\text{Pb}$  systematics of Allende CAIs: Canonical solar initial  $^{26}\text{Al}/^{27}\text{Al}$  ratio reinstated. *Earth Planet. Sci. Lett.* 272: 353–364.
- Janney P.E., Richter F.M., Mendybaev R.A., Wadhwa M., Georg R.B., Watson E.B. and Hines R.R. (2011) Matrix effects in the analysis of Mg and Si isotope ratios in natural and synthetic glasses by laser ablation-multicollector ICPMS: A comparison of single- and double-focusing mass spectrometers. *Chem. Geol.* 281: 26–40.
- Jones R.H. and Scott E.R.D. (1989). Petrology and thermal history of type IA chondrules in the Semarkona (LL3. 0) chondrite. In: *Proceedings of the 19th Lunar and Planetary Science Conference*. pp. 523–536.
- Jones R.H., Leshin L.A., Guan Y., Sharp Z.D., Durakiewicz T. and Schilk A.J. (2004) Oxygen isotope heterogeneity in chondrules from the Mokoia CV3 carbonaceous chondrite. *Geochim. Cosmochim. Acta* 68: 3423–3438.

- Krot A.N., Petaev M.I. and Yurimoto H. (2004) Amoeboid olivine aggregates with low-Ca pyroxenes: A genetic link between refractory inclusions and chondrules? *Geochim. Cosmochim. Acta* 68: 1923–1941.
- Krot A.N., Yurimoto H., Hutcheon I.D., Chaussidon M., MacPherson G.J. and Paque J. (2007) Remelting of refractory inclusions in the chondrule-forming regions: Evidence from chondrule-bearing type C calcium-aluminum-rich inclusions from Allende. *Meteorit. Planet. Sci.* 42: 1197–1219.
- Krot A.N., Amelin Y., Bland P., Ciesla F.J., Connelly J., Davis A.M., Huss G.R., Hutcheon I.D., Makide K., Nagashima K. and Nyquist L.E. (2009) Origin and chronology of chondritic components: A review. *Geochim. Cosmochim. Acta* 73: 4963–4997.
- Krot A.N., Nagashima K., van Kooten E.M.M. and Bizzarro M. (2017) Calcium-aluminum-rich inclusions recycled during formation of porphyritic chondrules from CH carbonaceous chondrites. *Geochim. Cosmochim. Acta* 201: 185–223.
- Kita N.T., Nagahara H., Togashi S. and Morishita Y. (2000) A short duration of chondrule formation in the solar nebula: Evidence from  $^{26}\text{Al}$  in Semarkona ferromagnesian chondrules. *Geochim. Cosmochim. Acta* 64: 3913–3922.
- Kita N.T., Ushikubo T., Knight K.B., Mendybaev R.A., Davis A.M., Richter F.M. and Fournelle J.H. (2012) Internal  $^{26}\text{Al}$ – $^{26}\text{Mg}$  isotope systematics of a Type B CAI: remelting of refractory precursor solids. *Geochim. Cosmochim. Acta* 86: 37–51.
- Larsen K.K., Trinquier A., Paton C., Schiller M., Wielandt D., Ivanova M.A., Connelly J.N., Nordlund Å., Krot A.N. and Bizzarro M. (2011) Evidence for magnesium isotope

- heterogeneity in the solar protoplanetary disk. *Astrophys. J. Lett.* 735.  
DOI:10.1088/2041-8205/735/2/L37
- Lee T. and Papanastassiou D.A. (1974) Mg isotopic anomalies in the Allende meteorite and correlation with O and Sr effects. *Geophys. Res. Lett.* 1: 225–228.
- Lee T., Papanastassiou D.A. and Wasserburg G.J. (1976) Demonstration of  $^{26}\text{Mg}$  excesses in Allende and evidence for  $^{26}\text{Al}$ . *Geophys. Res. Lett.* 3: 109–112.
- Libourel G. and Chaussidon M. (2011) Oxygen isotopic constraints on the origin of Mg-rich olivines from chondritic meteorites. *Earth Planet. Sci. Lett.* 301: 9–21.
- Libourel G. and Portail M. (2018) Chondrules as direct thermochemical sensors of solar protoplanetary disk gas. *Sci. Adv.* 4: eaar3321.
- Libourel G., Krot A.N. and Tissandier L. (2006) Role of gas-melt interaction during chondrule formation. *Earth Planet. Sci. Lett.* 251: 232–240.
- Ludwig K. (2008) Isoplot version 4.15: a geochronological toolkit for microsoft Excel. Berkeley Geochronology Center, Special Publication 4: 247–270.
- Luu T.H., Chaussidon M., Mishra R.K., Rollion-Bard C., Villeneuve J., Srinivasan G. and Birck J.L. (2013) High precision Mg isotope measurements of meteoritic samples by secondary ion mass spectrometry. *J. Anal. Atom. Spectrom.* 28: 67–76.
- Luu T.H., Young E.D., Gounelle M. and Chaussidon M. (2015) Short time interval for condensation of high-temperature silicates in the solar accretion disk. *Proc. Natl. Acad. Sci.* 112: 1298–1303.

- Luu T.H., Hin R.C., Coath C.D., Elliott T. (2019) Bulk chondrite variability in mass independent magnesium isotope compositions – Implications for initial solar system  $^{26}\text{Al}/^{27}\text{Al}$  and the timing of terrestrial accretion. *Earth Planet. Sci. Lett.* 522: 166–175.
- Mahan B., Moynier F., Siebert J., Gueguen B., Agranier A., Pringle E.A., Bollard J., Connelly J.N. and Bizzarro M. (2018) Volatile element evolution of chondrules through time. *Proc. Natl. Acad. Sci.* 115: 8547–8552.
- Marrocchi Y., Euverte R., Villeneuve J., Batanova V., Welsch B., Ferrière L. and Jacquet E. (2019a) Formation of CV chondrules by recycling of amoeboid olivine aggregate-like precursors. *Geochim. Cosmochim. Acta.* 247: 121–141.
- Marrocchi Y., Villeneuve J., Jacquet E., Piralla M., Chaussidon M. (2019b) Rapid condensation of the first Solar System solids. *Proc. Natl. Acad. Sci.* 116: 23461–23466.
- Mendybaev R.A., Richter F.M., Georg R.B., Janney P.E., Spicuzza M.J., Davis A.M. and Valley J.W. (2013) Experimental evaporation of Mg- and Si-rich melts: Implications for the origin and evolution of FUN CAIs. *Geochim. Cosmochim. Acta* 123: 368–384.
- Mishra R.K. and Chaussidon M. (2014) Timing and extent of Mg and Al isotopic homogenization in the early inner Solar System. *Earth Planet. Sci. Lett.* 390: 318–326.
- Morris M.A. and Boley A.C. (2018) Formation of chondrules by shock waves. In *Chondrules*. Eds. S. Russell, A. Krot and H. C. Connolly Jr. Cambridge U. Press. pp. 375–399.
- Nagashima K., Krot A.N., and Park C. (2015) An amoeboid olivine aggregate surrounded by an igneous ferroan olivine-rich rim from CO3.0 chondrite DOM 08006. *Lunar and Planetary Science Conference* 46, #2477.

- Nagashima K., Libourel G., and Krot A.N. (2019) Oxygen isotope systematics in a compound amoeboid olivine aggregate – chondrule object from Acfer 094 meteorite: implications to O-isotope exchange between melt and gas during chondrule formation. Lunar and Planetary Science Conference 50, #2167.
- Nagashima K., Thomen A., Krot A.N., Huss G.R., Kim N.K. and Park C. (2020) Investigation of instrumental fractionation in SIMS analyses of magnesium, silicon, and oxygen isotopes in silicates and oxides. Lunar and Planetary Science Conference 51, #1719.
- Niederer F.R. and Papanastassiou D.A. (1984) Ca isotopes in refractory inclusions. *Geochim. Cosmochim. Acta* 48: 1279–1293.
- Olsen M.B., Wielandt D., Schiller M., Van Kooten E.M. and Bizzarro M. (2016) Magnesium and  $^{54}\text{Cr}$  isotope compositions of carbonaceous chondrite chondrules—Insights into early disk processes. *Geochim. Cosmochim. Acta* 19: 118–138.
- Pack A., Yurimoto H. and Palme H. (2004) Petrographic and oxygen-isotopic study of refractory forsterites from R-chondrite Dar al Gani 013 (R3. 5–6), unequilibrated ordinary and carbonaceous chondrites. *Geochim. Cosmochim. Acta* 68: 1135–1157.
- Pringle E.A., Moynier, F., Beck P., Paniello R. and Hezel D.C. (2017) The origin of volatile element depletion in early solar system material: Clues from Zn isotopes in chondrules. *Earth Planet. Sci. Lett.* 468: 62–71.
- Richter F.M. (2004) Timescales determining the degree of kinetic isotope fractionation by evaporation and condensation. *Geochim. Cosmochim. Acta* 68: 4971–4992.



- Rudraswami N.G., Ushikubo T., Nakashima D. and Kita N.T. (2011) Oxygen isotope systematics of chondrules in the Allende CV3 chondrite: high precision ion microprobe studies. *Geochim. Cosmochim. Acta* 75: 7596–7611.
- Russell S.S., Krot A.N., Huss G.R., Keil K., Itoh S., Yurimoto H. and MacPherson G.J. (2005) The genetic relationship between refractory inclusions and chondrules. In *Chondrites and the Protoplanetary Disk* (Vol. 341, p. 317).
- Russell S.S., Connolly Jr H.C. and Krot A.N. (2018) *Chondrules: Records of Protoplanetary Disk Processes* (Vol. 22). Cambridge University Press.
- Ryu J.S., Vigier N., Decarreau A., Lee S.W., Lee K.S., Song H. and Petit S. (2016) Experimental investigation of Mg isotope fractionation during mineral dissolution and clay formation. *Chem. Geol.* 445: 135–145.
- Schiller M., Connelly J.N., Glad A.C., Mikouchi T., Bizzarro M. (2015) Early accretion of protoplanets inferred from a reduced inner solar system  $^{26}\text{Al}$  inventory. *Earth Planet. Sci. Lett.* 420: 45–54.
- Simon J.I., Young E.D., Russell S.S., Tonui E.K., Dyl K.A., Manning C.E. (2005) A short timescale for changing oxygen fugacity in the solar nebula revealed by high-resolution  $^{26}\text{Al}$ - $^{26}\text{Mg}$  dating of CAI rims. *Geochim. Cosmochim. Acta* 238: 272–283.
- Sio C.K.I., Dauphas N., Teng F.Z., Chaussidon M., Helz R.T. and Roskosz M. (2013) Discerning crystal growth from diffusion profiles in zoned olivine by in situ Mg–Fe isotopic analyses. *Geochim. Cosmochim. Acta* 123: 302–321.

- Soulié C., Libourel G. and Tissandier L. (2017) Olivine dissolution in molten silicates: An experimental study with application to chondrule formation. *Meteorit. Planet. Sci.* 52: 225–250.
- Teng F.Z., Li W.Y., Ke S., Marty B., Dauphas N., Huang S., Wu F.Y. and Pourmand A. (2010) Magnesium isotopic composition of the Earth and chondrites. *Geochim. Cosmochim. Acta* 74: 4150–4166.
- Teng F.Z., Wadhwa M. and Helz R.T. (2007) Investigation of magnesium isotope fractionation during basalt differentiation: implications for a chondritic composition of the terrestrial mantle. *Earth Planet. Sci. Lett.* 261: 84–92.
- Tenner T. J., Ushikubo T., Kurahashi E., Kita N. T. and Nagahara H. (2013) Oxygen isotope systematics of chondrule phenocrysts from the CO3.0 chondrite Yamato 81020: evidence for two distinct oxygen isotope reservoirs. *Geochim. Cosmochim. Acta* 102: 226–245.
- Ushikubo T., Nakashima D., Kimura M., Tenner T.J., Kita N. (2013) Contemporaneous formation of chondrules in distinct oxygen isotope reservoirs. *Geochim. Cosmochim. Acta* 109: 280–295.
- van Kooten E.M., Wielandt D., Schiller M., Nagashima K., Thomen A., Larsen K.K., Olsen M.B., Nordlund Å., Krot A.N. and Bizzarro M. (2016) Isotopic evidence for primordial molecular cloud material in metal-rich carbonaceous chondrites. *Proc. Natl. Acad. Sci.* 113: 2011–2016.

- van Kooten E. and Moynier F. (2019) Zinc isotope analyses of singularly small samples (<5 ng Zn): Investigating chondrule-matrix complementarity in Leoville. *Geochim. Cosmochim. Acta* 261: 248–268.
- van Kooten M.M.E., Moynier F. and Agranier A. (2019) A unifying model for the accretion of chondrules and matrix. *Proc. Natl. Acad. Sci.* 116: 18860–18866.
- Villeneuve J., Chaussidon M. and Libourel G. (2009) Homogeneous distribution of  $^{26}\text{Al}$  in the solar system from the Mg isotopic composition of chondrules. *Science* 325: 985–988.
- Villeneuve J., Chaussidon M. and Libourel G. (2011) Magnesium isotopes constraints on the origin of Mg-rich olivines from the Allende chondrite: Nebular versus planetary?. *Earth Planet. Sci. Lett.* 301: 107–116.
- Villeneuve J., Libourel G. and Soulié C. (2015). Relationships between type I and type II chondrules: Implications on chondrule formation processes. *Geochim. Cosmochim. Acta* 160: 277–305.
- Wasserburg G.J., Wimpenny J. and Yin Q.Z. (2012) Mg isotopic heterogeneity, Al-Mg isochrons, and canonical  $^{26}\text{Al}/^{27}\text{Al}$  in the early solar system. *Meteorit. Planet. Sci.* 47: 1980–1997.
- Weinbruch S., Zinner E.K., El Goresy A., Steele I.M. and Palme H. (1993) Oxygen isotopic composition of individual olivine grains from the Allende meteorite. *Geochim. Cosmochim. Acta* 57: 2649–2661.

- Young E. D., Ash R. D., Galy A. and Belshaw N. S. (2002a) Mg isotope heterogeneity in the Allende meteorite measured by UV laser ablation-MC-ICPMS and comparison with O isotopes. *Geochim. Cosmochim. Acta* 66: 683–698.
- Young E.D., Galy A. and Nagahara H. (2002b) Kinetic and equilibrium mass-dependent isotope fractionation laws in nature and their geochemical and cosmochemical significance. *Geochim. Cosmochim. Acta* 66: 1095–1104.
- Young E. D., Simon J. I., Galy A., Russell S. S., Tonui E. and Lovera O. (2005) Supra-canonical  $^{26}\text{Al}/^{27}\text{Al}$  and the residence time of CAIs in the solar protoplanetary disk. *Science* 308: 223–227.
- Yu Y., Hewins R.H. and Wang J. (2003) Experimental study of evaporation and isotopic mass fractionation of potassium in silicate melts. *Geochim. Cosmochim. Acta* 67: 773–786.
- Yurimoto H., Krot A.N., Choi B.G., Aléon J., Kunihiro T., Brearley A.J. (2008) Oxygen isotopes of chondritic components. *Rev. Mineral. Geochem.* 68: 141–186.

### Supplementary figures

**Fig. S1.** Elemental images of the studied chondrules (**A-C**) and melilite (**D**) from the Allende CV3 chondrite. The SIMS spots of 8-10  $\mu\text{m}$  for chondrules B-Ch5 and C-Ch1 are shown.

**Fig. S2.** Elemental images of the studied chondrules (**A-C**), amoeboid olivine aggregates (AOAs; **D**) and Ca- and Al-rich inclusions (CAIs; **E-G**) from the Leoville CV3 chondrite. The laser ablation spots of 40  $\mu\text{m}$  have been shown by the yellow circles.

**Supplementary data tables**

**Table S1** Chemical and Mg isotopic compositions of the used standards.

**Table S2** Analytical parameters of laser system and mass spectrometry.

**Table S3** Chemical and Mg isotopic compositions of olivine/glass standards and Allende chondrules measured with laser fluence of 3.37 J/cm<sup>2</sup> and spot size of 40 µm.

**Table S4** Chemical and Mg isotopic compositions of olivine/glass standards and Leoville chondrules measured with laser fluence of 4.23 J/cm<sup>2</sup> and spot size of 40 µm.

**Table S5** Chemical and Mg isotopic compositions of glass standards measured with laser fluence of 4.05 J/cm<sup>2</sup> and spot size of 110 µm.

**Table S6** Chemical and Mg isotopic compositions of glass standards measured with laser fluence of 11.47 J/cm<sup>2</sup> and spot size of 65 µm.

**Table S7** Literature bulk Mg isotopic compositions of AOAs and chondrules.

**Table S8** Mg evaporation rates inferred from experimental results in literature.

Table 1 Chemical and Mg isotopic composition of the standards, with CMAS glasses from this study and others from Chaussidon et al. (2017).

Sample	Type		Al <sub>2</sub> O <sub>3</sub> wt%	MgO wt%	SiO <sub>2</sub> wt%	<sup>44</sup> Ca/ <sup>24</sup> Mg <sup>a</sup>	<sup>48</sup> Ti/ <sup>24</sup> Mg <sup>a</sup>	<sup>52</sup> Cr/ <sup>26</sup> Mg <sup>a</sup>	δ <sup>25</sup>
									Mg (‰)
San Carlosolivi									-
olivine	ne	n.a.		48.88	40.91	0.0000	0.0000	0.0000	0.16
Ol synth Watsonolivi									-
#01	ne	n.a.		49.33	41.02	0.0000	0.0000	0.0000	0.62
Ol synth Watsonolivi									-
#02	ne	n.a.		49.33	41.02	0.0000	0.0000	0.0000	0.62
Ol synth Watsonolivi									-
#04	ne	n.a.		45.02	40.00	0.0000	0.0000	0.0000	0.62
Ol synth Watsonolivi									-
#05	ne	n.a.		40.22	38.88	0.0000	0.0000	0.0000	0.62
Ol synth Watsonolivi									-
#06	ne	n.a.		32.83	37.14	0.0000	0.0000	0.0000	0.62
	glass								-
StHs6/80-G		17.80	1.97	63.70	0.0509	0.1681	0.0051		0.18
	glass								-
BCR-2G		13.80	3.59	54.80	0.0382	0.2955	0.0030		0.16
	glass								-
TB-1G		16.70	3.70	54.30	0.0344	0.1133	0.0000		0.16
	glass								-
T1-G		17.10	3.75	58.60	0.0359	0.0948	0.0033		0.15
	glass								-
ML3B-G		13.60	6.59	51.40	0.0302	0.1522	0.0158		0.17
	glass								-
BHVO-2G		13.60	7.13	49.30	0.0303	0.1807	0.0232		0.12
	glass								-
KL2-G		13.30	7.34	50.30	0.0282	0.1642	0.0236		0.14
MORB	glass								-
(CLDR01RV)		15.32	8.70	49.94	0.0267	n.a.	n.a.		0.13
	glass								-
BIR-1G		15.60	9.37	47.30	0.0271	0.0464	0.0254		0.15
	glass								-
GOR132-G		11.00	22.40	45.50	0.0072	0.0064	0.0666		0.09
	glass								-
GOR128-G		9.91	26.00	46.10	0.0046	0.0052	0.0515		0.15
	glass								-
CMAS-synth-I		33.55	3.66	24.06	0.2008	0.0000	0.0000		1.99

	glass							-
CMAS-synth -II	31.49	4.99	26.20	0.1420	0.0000	0.0000	1.99	
	glass							-
CMAS-synth -III	27.03	9.23	31.11	0.0671	0.0000	0.0000	1.99	
	glass							-
CMAS-synth -IV	24.17	11.30	37.10	0.0461	0.0000	0.0000	1.99	

<sup>a</sup>Atomic ratios are given here.

**Declaration of interests**

☒ The authors declare that they have no known competing financial interests or personal relationships that could have appeared to influence the work reported in this paper.

☐ The authors declare the following financial interests/personal relationships which may be considered as potential competing interests: